1994ApJ...424..905H

THE ASTROPHYSICAL JOURNAL, 424:905–923, 1994 April 1

ANALYSIS OF THE EARLY SPECTRA AND LIGHT CURVE OF SN 1987A

PETER H. HAUSCHILDT
Department of Physics and Astronomy, Arizona State University, Tempe, AZ 85287-1504;
yeti@sara.la.asu.edu

AND

LISA M. ENSMAN
Physics Department, University of Arizona, Tucson, AZ 85721;
lensman@as.arizona.edu
Received 1993 July 29; accepted 1993 October 6

ABSTRACT

Numerical modeling of supernova spectra, light curves, and hydrodynamics requires physical inputs, numerical techniques, approximations, and assumptions which must be thoroughly understood in order to study the details of supernova explosions. Here, we discuss some of these in the context of the early evolution of supernova 1987A. Gray radiation-hydrodynamics is used to calculate the bolometric light curve and the hydrodynamic evolution of the supernova. Synthetic spectra are then obtained for the resulting density and velocity structure. The spectrum calculations are performed using a special-relativistic treatment of the radiative transfer equation in the comoving frame, line blanketing by about 10^5 spectral lines, and departures from LTE for H I, He I, Mg II, and Ca II. We find that we are able to simultaneously fit the early light curve and spectra reasonably well, using a progenitor model from Arnett (1991a), without fine-tuning the free parameters. Temperature structures and radiative equilibrium, non–LTE effects, homologous expansion, and mean opacities are discussed.

Subject headings: hydrodynamics — radiative transfer — supernovae: individual (SN 1987A)

1. INTRODUCTION

This paper describes the first results from an ongoing study of the physics underlying spectrum formation and light curve evolution in core-collapse supernovae. In this study, we hope to verify the acceptability of several simplifications and assumptions which will eventually allow us to compute a fully self-consistent and complete supernova model—one which fits light curves, spectra, and hydrodynamics and does not neglect any important physics. As we will describe in more detail below, we use here the results of a gray radiation-hydrodynamics simulation as input for stellar atmosphere-type modeling of the spectrum of SN 1987A at various epochs. We then analyze the results of the atmosphere calculations to investigate departures from LTE, opacity averages, and velocity field effects. In future work, we will discuss these and other issues in more depth, and incorporate the most important improvements and/or simplifications into supernova models. Our motivation is to, ultimately, use the techniques of radiation-hydrodynamics and spectral synthesis simultaneously by using a spectrum code to compute accurate mean opacities for a gray radiation-hydrodynamics code *at each time step*, or, even better, by doing full frequency-dependent radiation-hydrodynamics.

As a by-product of this work, we obtain a model for the first few days of SN 1987A which fits both the light curve and spectra quite well. Note, however, that this fit has not been optimized. It is not our goal here to achieve the best fit possible, but rather to investigate the fundamental physics of the interaction of a nongray radiation field with the hydrodynamical evolution of the expanding ejecta. We, therefore, present results for only one specific model and discuss not only the light curve and spectra, but also the evolving structure of the model atmosphere and some important physical effects.

1.1. *Supernova 1987A*

SN 1987A was discovered in the Large Magellanic Cloud on 1987 February 23/24, by I. Shelton and A. Jones (IAUC 4316, 1987). The progenitor was the blue supergiant (spectral class B3Ia) Sanduleak −63°202. The high quality of the observations interested several groups in modeling the spectrum of this bright Type II.

Lucy (1987a, b) used a Schuster-Schwarzschild model for the envelope and solved the radiative transfer equation (RTE) in the comoving frame (CMF) using a Monte Carlo method, including metal lines in the nonrelativistic Sobolev approximation.

Höflich (1987) has published synthetic spectra for SN 1987A using pure hydrogen envelopes and a nonrelativistic treatment of the radiative transfer, including departures from local thermodynamic equilibrium (LTE). In later work (Höflich 1988, 1990) he included metal line blanketing in the pure scattering approximation as well as advection and aberration terms in the solution of the radiative transfer for lines. However, he did not consider the influence of the expansion velocity on the continuum transfer or on the temperature structure.

Eastman & Kirshner (1989) solved the RTE in the CMF, for lines and continua, neglecting the Lagrangian time derivative; i.e., they set $D/Dt \equiv 0$, ignoring the curvature of the light rays due to the velocity field. (The assumption of $\partial/\partial t \equiv 0$ is usually well justified.) They computed LTE radiative equilibrium models and included metal lines in the pure scattering approximation. Then they solved the non–LTE rate equations for H I and He I, using a nonrelativistic Sobolev approximation to compute radiative rates.

Schmutz et al. (1990) used an approach similar to Eastman & Kirshner. An LTE temperature was computed using the Monte Carlo radiative transfer method of Abbott & Lucy

(1985). With this fixed temperature structure, they then solved the non–LTE continuum and line transfer problems for H I and He I (consistently), using an accelerated Λ-operator iteration method. They solved the non–LTE line radiative transfer in the CMF, neglecting the advection and aberration terms, but the continuum radiative transfer used a static approximation. Both Schmutz et al. (1990) and Eastman & Kirshner (1989) took their density stratification from hydrodynamical calculations.

Although most of these authors did not include advection and aberration terms self-consistently in their calculations, it has been shown by Mihalas, Kunasz, & Hummer (1976) and Hauschildt & Wehrse (1991) that relativistic effects, *in particular both advection and aberration*, are very important at the velocities usually observed in SN II. In particular, the effect of advection and aberration on the temperature structure in an expanding shell is very large and cannot be neglected (Mihalas 1986; Hauschildt 1992b).

Another important physical effect which must be included is the coupling between departures from LTE, line blanketing, and the temperature structure of a SN II atmosphere. Results obtained by Hauschildt et al. (1992) for novae indicate that the effects of line blanketing, by metal lines in the UV, have a much larger influence on the temperature structure than do non–LTE effects. This becomes clear if one realizes that, for the conditions found in SN II's, most of the radiative energy is transported in the wavelength region from 1200 Å to 3500 Å. In this spectral region, the opacity is dominated by metal lines so that the influence of H I non–LTE on the temperature structure is small. Line blanketing also has a large effect on the departures from LTE—we present in this paper the results of calculations which show that metal-line blanketing has a major influence on the departures from LTE for H I, He I, Mg II, and Ca II. These considerations indicate that metal-line blanketing has to be included *self-consistently* in the solution of the multilevel non–LTE rate equations for these species in order to obtain their correct line profiles. Otherwise, one cannot accurately determine, for example, the abundances of the elements from observed spectra.

The remainder of this paper is organized as follows: In § 2 we describe briefly the numerical methods used for the radiation-hydrodynamical simulation and the stellar atmosphere calculations. In § 3, we discuss the general results and the structure of the photosphere, and the synthetic spectra are compared to observations of SN 1987A in the UV and optical spectral ranges. Section 4 is devoted to a summary and a discussion of the results.

2. NUMERICAL METHODS

2.1. *Radiation Hydrodynamics*

The hydrodynamics and the bolometric light curve for our simulation were computed using the radiation-hydrodynamics (hereafter, rad-hydro) code VISPHOT (Ensman 1991; Ensman & Burrows 1992). This code solves the frequency-integrated moment equations of the radiative transfer equation in the comoving frame (see Mihalas & Mihalas 1984) to $O(v/c)$, assuming spherical symmetry and LTE. In other words, it solves the gas momentum equation, the continuity equation, the radiating fluid (gas + radiation) energy equation, the radiation energy equation, and the radiation momentum equation to obtain $\rho(r, t)$, $v(r, t)$, $T_{\rm gas}(r, t)$, $E_{\rm rad}(r, t)$, and $F(r, t)$. Here, ρ is the gas density, v is the velocity of the material, $T_{\rm gas}$ is the gas temperature, $E_{\rm rad}$ is the radiation energy density (which may be parameterized as $T_{\rm rad}$ via $E_{\rm rad} = aT_{\rm rad}^4$), and F is the radiative flux. The diffusion approximation is not made, thus no flux limiter is required and the solution is valid in both optically thick and optically thin regions. Nor is it assumed that the radiation and the gas are in equilibrium at a single temperature. The equations are closed with Eddington factors obtained from a separate solution of the time-independent gray radiative transfer equation.

In principle, one needs three different mean opacities to solve the rad-hydro equations:

$$\chi_F = \frac{\int \chi_\lambda F_\lambda d\lambda}{\int F_\lambda d\lambda} ,$$

$$\kappa_{\rm P} = \frac{\int \kappa_\lambda B_\lambda(T) d\lambda}{\int B_\lambda(T) d\lambda} ,$$

and

$$\kappa_J = \frac{\int \kappa_\lambda J_\lambda d\lambda}{\int J_\lambda d\lambda} ,$$

where χ_F is the flux mean of the total extinction χ_λ, $\kappa_{\rm P}$ is the Planck mean of the absorption coefficient κ_λ (i.e., of the absorptive component of the total opacity), and κ_J (or κ_E) is the energy mean of κ_λ. J is the mean intensity, F is the radiative flux, $B_\lambda(T)$ is Planck's function, and $\chi_\lambda = \kappa_\lambda + \sigma_\lambda$, where σ_λ is the scattering component of the total extinction. In optically thick regions, where the diffusion approximation applies, χ_F becomes equal to the Rosseland mean opacity $\chi_{\rm R}$, and κ_J becomes equal to $\kappa_{\rm P}$. Note that neither χ_F nor κ_J can be computed without knowing the complete wavelength-dependent spectrum of the radiation field.

In the rad-hydro simulation discussed below, it was assumed that $\chi_F = \chi_{\rm R}$ and $\kappa_J = \kappa_{\rm P}$. The Rosseland mean opacities were obtained from a fit by Arnett (1991b) based on tables from Cox & Stewart (1970a, b). For the Planck means, which are important in determining the temperature structure, we were forced to assume that $\kappa_{\rm P} = \chi_{\rm R} - \sigma_e$, where σ_e is the electron scattering opacity. This is clearly a crude approximation, since $\kappa_{\rm P}$ can actually be 1 to 2 orders of magnitude *larger* than the Rosseland mean in relevant regimes (see Ensman, Hauschildt, & Allard 1993). However, the light curve, densities, and velocities are not expected to be very sensitive to $\kappa_{\rm P}$, so the basic model obtained should be acceptable for our purposes.

Another effect is the change of the opacity due to the large velocity gradient (Karp et al. 1977). See, e.g., Müller & Höflich (1991), Höflich, Müller, & Khokhlov (1993), Eastman et al. (1993) for supernova models computed including an approximate "expansion opacities." Later in this paper we will briefly discuss the effects of the velocity field on the Lagrangian frame averaged extinction and absorption coefficients we found in our calculations.

2.2. *Spectral Synthesis*

The spectral synthesis is done using a method similar to that described in detail by Hauschildt et al. (1992). We give here only a brief description of the techniques used, including recent improvements.

The expanding stellar atmospheres code PHOENIX solves, self-consistently, the spherically symmetric, nongray, special-relativistic, CMF equations of radiative transfer and radiative equilibrium (hereafter, the SSRTE and the RE equation), coupled with the multilevel, non–LTE rate equations. The version of PHOENIX described by Hauschildt et al. (1992) for nova atmosphere calculations used the discrete ordinate matrix exponential (DOME) method (Hauschildt & Wehrse 1991) for the solution of the SSRTE and the RE equation. The equivalent two-level-atom (ETLA) method (e.g., Mihalas 1978) was used to obtain the solution of the multilevel non–LTE rate equations. The numerical stability and the performance of PHOENIX have recently been greatly improved by incorporating the following changes (Hauschildt et al. 1994): (i) the solution of the SSRTE is now obtained using the accelerated lambda iteration (ALI) technique, as described by Hauschildt (1992a and references therein), (ii) the RE equation is solved using the hybrid (ALI combined with partial linearization) method given by Hauschildt (1992b), and (iii) the multilevel non–LTE continuum and line transfer problem is treated using the ALI method described in Hauschildt (1993).

Presently, we treat the following species in non–LTE: H I with 10 levels, using atomic data for radiative and collisional transitions given by Johnson (1972), He I with 11 levels (Baron & Hauschildt 1994, in preparation), Mg II with three levels (Shine 1978), and Ca II with five levels (Shine & Linsky 1978). The Mg II model atom is representative for the formation of the $h + k$ lines, and the Ca II model atom is sufficient for the calculation of the H + K lines and the Ca II infrared triplet.

In addition to the non–LTE lines, the models include line blanketing by the most important $\sim 10^5$ metal lines selected from the line list of Kurucz & Peytremann (1975) with an updated Fe II line list (Kurucz 1988). See Hauschildt et al. (1992) for details. We treat line scattering of the metal lines approximately by parameterizing the albedo for single scattering. The calculation of the albedo, α, would require a full non–LTE treatment of all lines and continua, which is outside the scope of this paper, therefore, we adopt an average value of $\alpha = 0.95$ for all metal lines. Tests have shown that, due to the large velocity gradient in the supernova photospheres, the shapes of the lines do not depend sensitively on α, making our approach a reasonable first approximation.

All of the non–LTE lines included (~ 50) are represented by depth-dependent Gaussian profiles with 25 wavelength points per line. In total, ~ 5000 wavelength points are used for lines and continua. We have assumed here a statistical velocity of $\xi = 1000$ km s^{-1} $\sim 0.03 v_{\max}$ (treated as isotropic, Gaussian-shaped line broadening). Physically, such broadening might be produced by a collection of blobs (created by Rayleigh-Taylor instabilities) having the same composition but a range of velocities. Numerically, it permits the use of fewer frequency points in the spectrum calculations. Test calculations (Ensman et al. 1993) have shown that the results are insensitive to this parameter as long as the expansion velocities are significantly larger than ξ, a condition which is fulfilled in the models discussed below. (We consider only the first few days after shock breakout when velocities near the photosphere are over 10,000 km s^{-1}.)

Continuum absorption and scattering coefficients are calculated using the species and cross sections given in Hauschildt et al. (1992). The ionization stages I–III of C, N, O, Si, S, Fe, Al, Na, K, Ti, Sc, Mn, and Cr are included in LTE in the solution of the generalized equation of state using the method described in Hauschildt (1993).

2.3. *Calculation of the Model Atmospheres and the Synthetic Spectra*

To calculate a synthetic spectrum, one must specify the emergent bolometric luminosity, the composition, the velocity, the electron temperature, and the gas pressure (or density) as functions of radius. A time-step of the rad-hydro model sequence (hereafter, a "snapshot") gives the complete structure of the SN envelope, including all of the abovementioned quantities, thus it could, in principle, be used to solve the multilevel non–LTE continuum and line transfer problem and compute a synthetic spectrum. However, the gas temperature and pressure are subject to some systematic problems: (i) the Planck mean opacities used in *this* rad-hydro calculation were rough approximations (see § 2.1), thus the temperature structure obtained cannot be assumed to be completely accurate, (ii) the use of gray opacities in the rad-hydro code does not describe the effects of nongray radiation transport and, therefore, the temperature structure as obtained from a *nongray* (even LTE) calculation will be different, and (iii) the gas pressures given by the rad-hydro code are calculated using electron and ion densities derived for LTE, but departures from LTE will change n_e, in particular in the vicinity of ionization regions in the photosphere. This can be important for the formation of both the continuum and the line spectrum due to the dominance of Thomson scattering in SN photospheres.

Therefore, we use PHOENIX to calculate a temperature structure (and the non–LTE population densities) using the assumption of radiative equilibrium in the *CMF* (i.e., no net absorption or emission by any gas element). We take $\rho(r)$ and $v(r)$, as well as the *emergent* luminosity in the Eulerian, or lab, frame from the rad-hydro snapshots. Note that this does *not* mean that the lab frame luminosity is constant in time or optical depth, but it is calculated as a function of time by the rad-hydro simulation and as a function of optical depth by the stellar atmosphere code (see Hauschildt 1992b for details). However, we do not iterate on the emergent lab frame luminosity by feeding the results of the atmosphere calculation back into the rad-hydro simulation. This would clearly change the results of the rad-hydro time sequence and is beyond the scope of this paper. The assumption of RE is usually well justified in the outer layers of the expanding envelope, as can be seen from the rad-hydro snapshots (see below). To check the influence of the temperature distribution on the departures from LTE and the synthetic spectra, we also use the rad-hydro temperature structure, $T_{\rm gas}$, to solve the non–LTE rate equations and to compute synthetic spectra for all snapshots.

The iteration for the structure of the model atmosphere proceeds as follows: Using the rad-hydro gas temperature and LTE population densities as initial guesses, we solve the generalized equation of state to compute the electron density and the level populations of all species considered in the calculation. Using the method described in Hauschildt et al. (1992 and references therein), the most important $\sim 10^5$ metal lines are then selected from the line list and used in the solution of the SSRTE. (This is repeated in each iteration cycle to account for changes in the temperatures and population densities.) The SSRTE is solved, using 2000 to 5000 wavelength points, and the radiative rates and the approximate rate operators are updated. These are subsequently used to update the departure coefficients in an ALI step for the rate equations. An improved temperature structure is computed and the cycle is repeated if the convergence criteria are not met. Typically 20 iterations are needed to obtain radiative equilibrium to better than 1% and to converge the departure coefficients to at least 0.1% (see also Hauschildt 1993). After the temperature structure and the non–LTE rate equations of a particular snapshot model atmosphere have converged, we compute a high-resolution

Eulerian-frame spectrum which we subsequently compare to the observed spectrum of the corresponding epoch.

The storage required for PHOENIX is about 50 MB (due to size of the line list), and about 2 hr CPU time (about 6 minutes per iteration) are needed on an IBM RS/6000-580 for a complete model atmosphere. Most of the CPU time is used for the calculation of the continuum (~30%) and metal-line (~50%) absorption coefficients for the ~3000 wavelength points. The solution of the SSRTE and the rate-equations (including the generalized equation of state) are highly optimized and take only about 20% of the CPU time.

2.4. *Model Parameters*

The most important parameters in our model for the early evolution of SN 1987A are (i) the initial model for the progenitor star, (ii) the explosion energy, (iii) the elemental abundances, and (iv) the epoch of the rad-hydro simulation used for a snapshot. The explosion energy and the structure of the progenitor together determine the final velocity, density, and temperature profiles of the ejecta. The abundances are, of course, crucial in the formation of the spectra. Here, we keep all these parameters, with the obvious exception of the epoch, fixed, i.e., we consider only one rad-hydro sequence and its corresponding spectral sequence.

The progenitor model, a 17.6 $M_\odot$ blue supergiant (originally 20 $M_\odot$ on the main sequence) with radius 3.2×10^{12} cm was obtained from a stellar evolution calculation by Arnett (1991a). An explosion energy of 1×10^{51} ergs was used to eject all but the inner 1.3 $M_\odot$, which was presumed to form a neutron star. See Ensman & Burrows (1992, model 500full1) for move information, as well as a detailed description of shock breakout. The hydrogen, helium, and metal mass fractions in the hydrogen envelope were $X = 0.67$, $Y = 0.32$, and $Z = 0.007$. *However*, for the spectral synthesis, $X = 0.74$, $Y = 0.25$, and $Z = 0.006$ were used, the metals having number abundances equal to $\frac{1}{3}$ their solar values. Details of the spectrum are not very sensitive to X and Y in this range.

3. RESULTS

3.1. *Bolometric Light Curve and Hydrodynamic Evolution*

The early bolometric light curve for our model, as computed by the rad-hydro code, is shown in Figure 1. Also shown are the times of the snapshots described below (asterisks) and SN 1987A data from Catchpole et al. (1987) (plus symbols). The conversion of bolometric luminosity to apparent magnitude assumed a distance modulus of 18.5 and included no reddening or extinction corrections. The fit to the shape of the observed bolometric light curve is quite good for the first 11–12 days. After that, the theoretical curve begins to rise more slowly than the observations. This may indicate the need for mixing in the ejecta (a gradient in the helium abundance, for example, would change the opacities and thus the light curve—e.g., Woosley 1988), a slightly different initial density structure in the initial model, or simply better opacities. On the other hand, a full non–LTE, multiwavelength calculation of the light curve might be required to improve the fit to the observed light curve.

The bright spike at the beginning of the light curve is "shock breakout." Details of this time period can be found in Ensman & Burrows (1992). In summary, the sequence of events which occurs is as follows: As the shock wave created at the core of the star following core collapse reaches the photosphere of the progenitor, it becomes a supercritical radiating shock (see Mihalas & Mihalas 1984 and references therein) with a radiative precursor. As the radiation from the shock front, i.e., the precursor, breaks through the photosphere, we see a sudden jump in luminosity which is referred to as "shock" breakout or the UV burst. The huge flux of radiation which pours through the final portion of unshocked gas preheats and preaccelerates

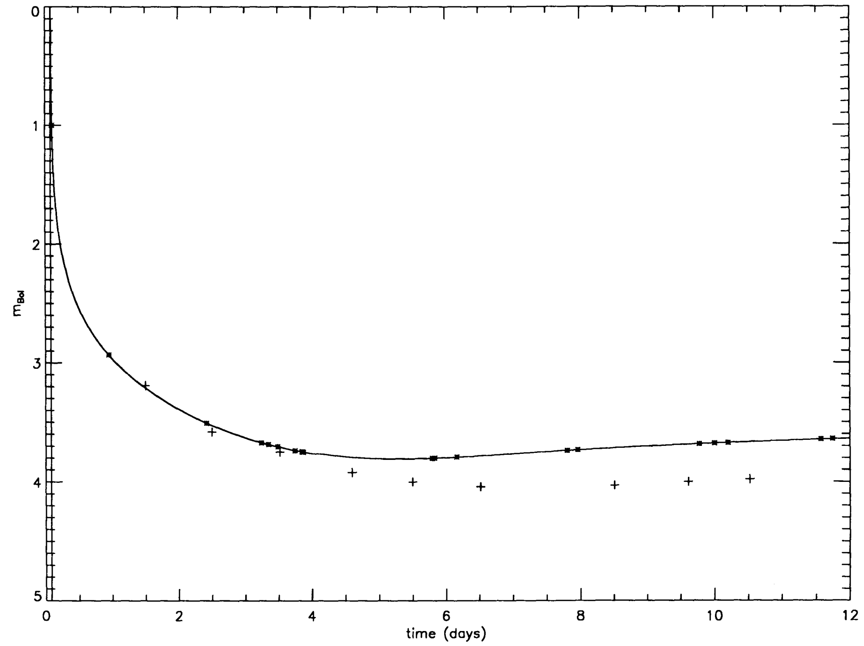

FIG. 1.—The early bolometric light curve of SN 1987A compared to the results of the rad-hydro simulation. The observations were taken from Catchpole et al. (1987) (*plus symbols*). The full curve gives the bolometric magnitudes obtained by the rad-hydro simulation and the asterisks give the epochs for which we have calculated snapshot model atmospheres. We have assumed a distance modulus of 18.5 mag, corresponding to a distance of 50 kpc of SN 1987A.

it, so much so that, before the shock can actually exit the star, it simply dissipates. That is, the gas ahead of the front experiences enough radiative acceleration to reach a velocity equal to the post-shock velocity, erasing any discontinuity which one could call a shock.

However, not all of the gas ahead of the shock front receives the same amount of preacceleration. The material farther out finds itself moving a bit slower than the material farther in, hence compression occurs and a new shock front is born, this time in an optically thin region. Since the gas is free to radiate its energy away, compression behind the shock front results in little or no temperature increase, and the density rises by a few orders of magnitude. A very thin, dense shell forms, containing only $1.3 \times 10^{-6}\ M_\odot$ in this case. If no circumstellar material is included (as in our model), this shock eventually reaches the edge of the star (the grid) and disappears, leaving a small density inversion at the former inner edge of the thin, dense shell.

As the original shock from the core radiates away all of its energy away and vanishes, the observed bolometric luminosity quickly falls. Internal energy, mainly trapped radiation, then begins to power the light curve as it diffuses out of the ejecta. High fluxes continue to radiatively accelerate the gas until homologous expansion ($v \propto r$) is reached at about 1.3 days (except at the very center of the ejecta where radioactive decay energy continues to accelerate overlying material). When the temperature at the surface of the expanding envelope reaches about 6000 K, hydrogen begins to recombine. A true recombination front forms at about 3.5 days. Later evolution of the light curve is determined by the interaction of this recombination front, which moves inward in mass, with the outward diffusion of energy deposited by radioactive decay of ^{56}Ni and its daughter ^{56}Co.

3.2. *Structure of the Photosphere*

By examining the structure of the ejecta at different stages in the outburst, we can test the accuracy of some of the assumptions which are typically made in pure stellar atmosphere-type modeling of SN spectra, e.g., homologous expansion and power-law density profiles. We can also compare the temperature structure obtained with the rad-hydro code to that derived from the assumption of radiative equilibrium and observe the degree to which the gas is not in LTE.

In Figure 2 we display temperature, velocity, and density profiles and departure coefficients for the first levels of H I, Mg II, and Ca II at several epochs. In addition to the velocity itself, we include in the graphs the quantity ζ, which we define as

$$\zeta(r) = \frac{v_{\rm out}/r_{\rm out}}{v(r)/r} - 1 ,$$

where $v_{\rm out}$ and $r_{\rm out}$ are the velocity and radius of the outermost zone considered in the spectrum calculation. $\zeta(r)$ measures deviations from homologous expansion, $\zeta(r) \equiv 0$ corresponding to the case of pure homologous expansion. All quantities are plotted as functions of $\tau_{\rm std}$, the continuum optical depth in absorption at $\lambda = 5000$ Å. Note that this optical depth scale does not include contributions from scattering, particularly electron scattering, so $\tau_{\rm std} = 1$ does not correspond to "the" photosphere, rather it is more closely related to the thermalization depth. A Rosseland mean optical depth of unity occurs at $\tau_{\rm std} \sim 4 \cdots 9 \times 10^{-3}$, depending on the epoch. For most epochs considered here, the line-forming region extends down to $\tau_{\rm std} \sim 0.1$. The relation between $\tau_{\rm std}$ and the radial coordinate is *not* the same for each epoch but is recalculated for each model atmosphere.

Deviations of the velocity from homologous expansion can be large in the neighborhood of the photosphere during the earliest phases of the SN outburst. In the first snapshot presented in Figure 2 ($t = 2.45$ hr after core collapse), $\zeta(r)$ increases with optical depth, climbing to about 10% at the bottom of the line-forming region, and to more than 50% at $\tau_{\rm std} \approx 10^3$. At somewhat later epochs the differences become smaller, but, in contrast to the situation found earlier, both positive and negative deviations from homologous expansion exist. At $t = 1.2d$ (Fig. 2*b*), $\zeta(r)$ is less than 1%. For an expansion velocity of 30,000 km s^{-1}, a 1%–2% deviation amounts to only 300–600 km s^{-1}, which is too small to have any significant influence on the temperature structure or the emergent spectrum, in general, but the profiles of isolated, i.e., nonblended, lines may be sensitive to *systematic* velocity differences of this size. We conclude that, as one would expect, during the very early phases of the outburst (the first day for this model) the differences between the velocity field obtained by the rad-hydro simulation and the assumption of homologous expansion are large and certainly important for the formation of the spectrum.

The density structure of the rad-hydro simulation is at no epoch given by a single power law with respect to the radius. In the early phases, i.e., during the first 2.5 days after outburst, a density inversion, left over from the thin, dense shell formed during shock breakout, is apparent. It later leaves the optical depth grid used in the model atmospheres. This structure is also present in the run of the departure coefficients. The exponent N of a local fit to a power law of the form $\rho \propto r^{-N}$ is plotted in Figure 2. It shows that the density gradient is very large (N is off scale) in the outermost layers and shallower toward the center of the ejecta. For the earliest epochs, however, the density in the line and continuum-forming region can be approximated to good accuracy by a local power law. At later epochs, the radial extent of the line and continuum-forming regions is larger and deviations from a power-law density are more important for the formation of the spectrum.

Figure 2 also compares the temperature structure found by the rad-hydro code ($T_{\rm gas}$, solid lines) to that determined by PHOENIX using the condition of radiative equilibrium in the CMF ($T_{\rm RE}$, dotted lines). The difference between $T_{\rm gas}$ and $T_{\rm RE}$ in the outer parts of the atmosphere, which can be as large as several thousand degrees, is probably caused by differences in opacities and/or the treatment of the radiation in the rad-hydro and the stellar atmosphere codes, rather than a real lack of radiative equilibrium in the rad-hydro results. The gray radiative transfer used in VISPHOT cannot account for effects of wavelength redistribution of radiative energy or the effect of strong line-blanketing by Fe II in certain parts of the spectrum (in particular the UV range from 1000 Å to 3000 Å). Non-LTE effects on the temperature structure are relatively small compared to the much larger effects of line blanketing during the phase we consider here.

In deeper, optically thick layers, $T_{\rm gas}$ is much larger than $T_{\rm RE}$, implying that the gas is far from radiative equilibrium at those depths. Energy is still being exchanged between the moving plasma and the changing radiation field. However, these regions are too deep inside the atmosphere to have a significant influence on the emergent spectrum. Note that the RE temperature gradient here is much shallower than it would be

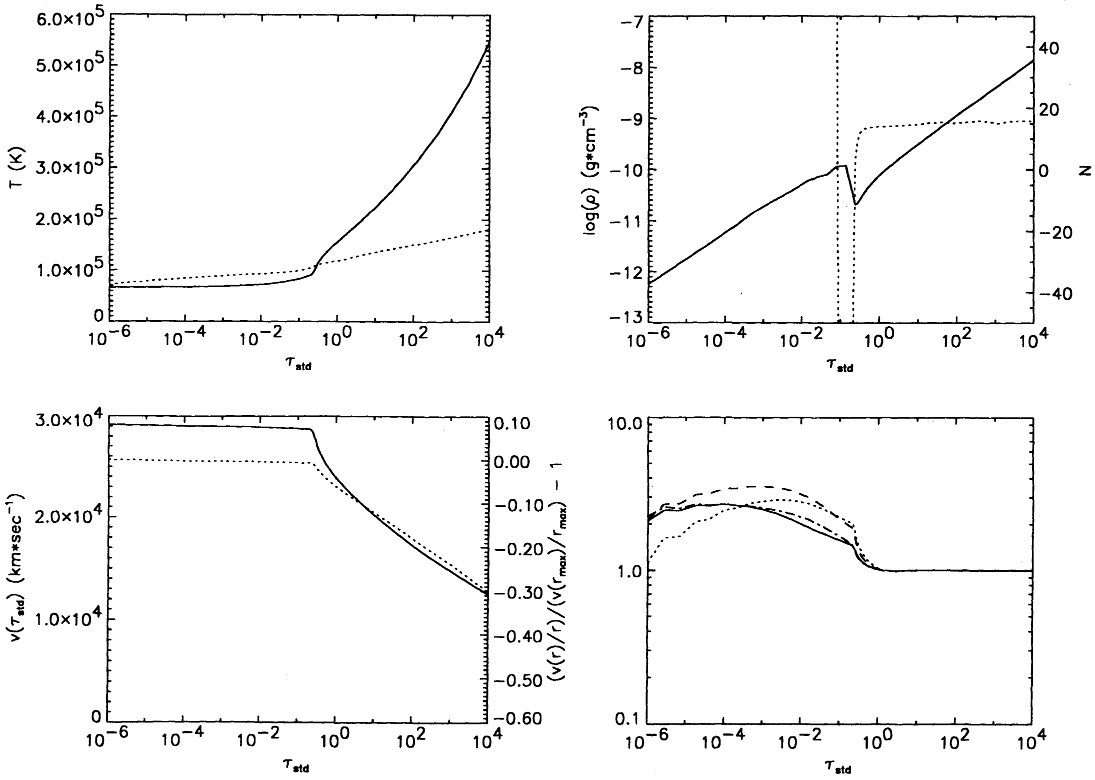

Fig. 2*a*

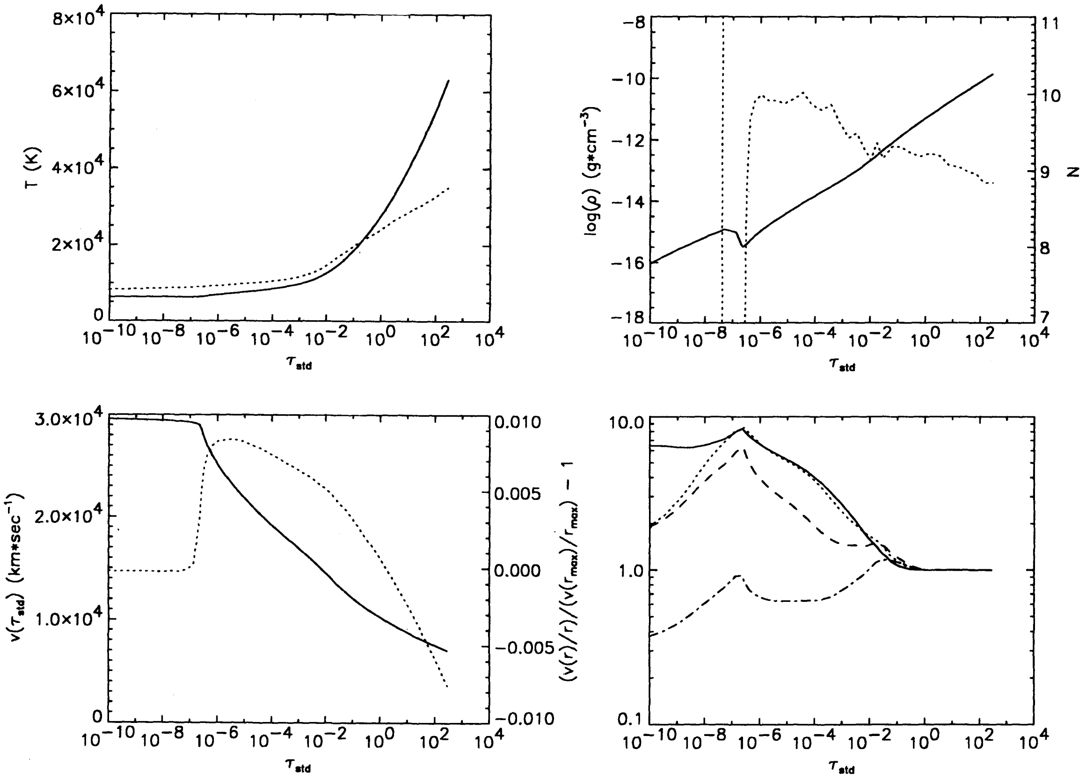

Fig. 2*b*

Fig. 2.—The structure of the model atmospheres corresponding to rad-hydro snapshots at $t = 2.45$ hr (*a*), 1.26 day (*b*), 2.09 day (*c*), and 3.85 day (*d*) after core collapse. For each epoch, the rad-hydro gas temperature profile (*solid curve*) is compared to the radiative equilibrium temperature profile (*dotted curve*) in the upper left plot. In the upper right-hand corner is the density (*full curve*) and the exponent N of a local power-law fit $\rho(r) \propto r^{-N}$ (*dotted curve*). The velocity field and the quantity ζ (see text) are shown in the lower left-hand graph. The lower right-hand graph shows the run of the ground state departure coefficients of H I (*full curve*), He I (*dotted curve*), Mg II (*dashed curve*), and Ca II (*dash-dotted curve*). The ordinate gives $\log_{10}(b_1)$ for the different species. The abscissa for all plots is $\tau_{\rm std}$, the optical depth in absorption in the continuum at 5000 Å.

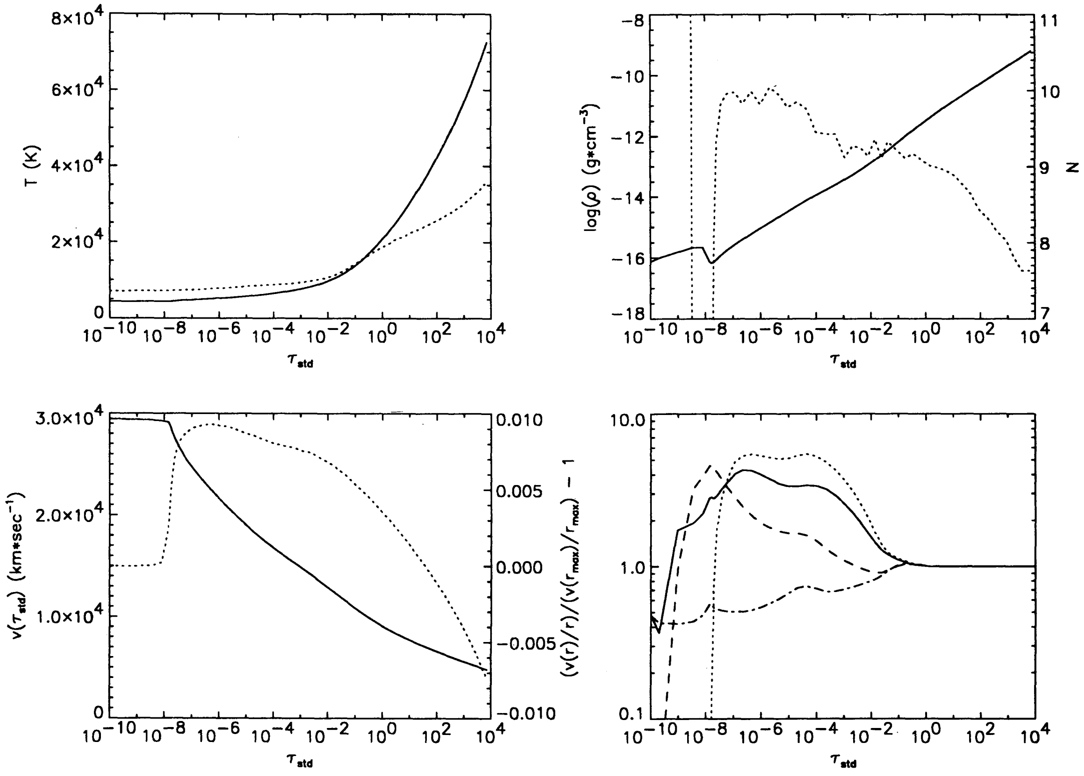
8×10^4
6×10^4
4×10^4
2×10^4
0
T (K)
10^-10 10^-8 10^-6 10^-4 10^-2 10^0 10^2 10^4
τ_std
-8
-10
-12
-14
-16
-18
log(ρ) (g*cm^-3)
11
10
9
8
7
N
3.0×10^4
2.0×10^4
1.0×10^4
v(τ_std) (km*sec^-1)
0.010
0.005
0.000
-0.005
-0.010
(v(r)/r)/(v(r_max)/r_max) - 1
10.0
1.0
0.1

FIG. 2c

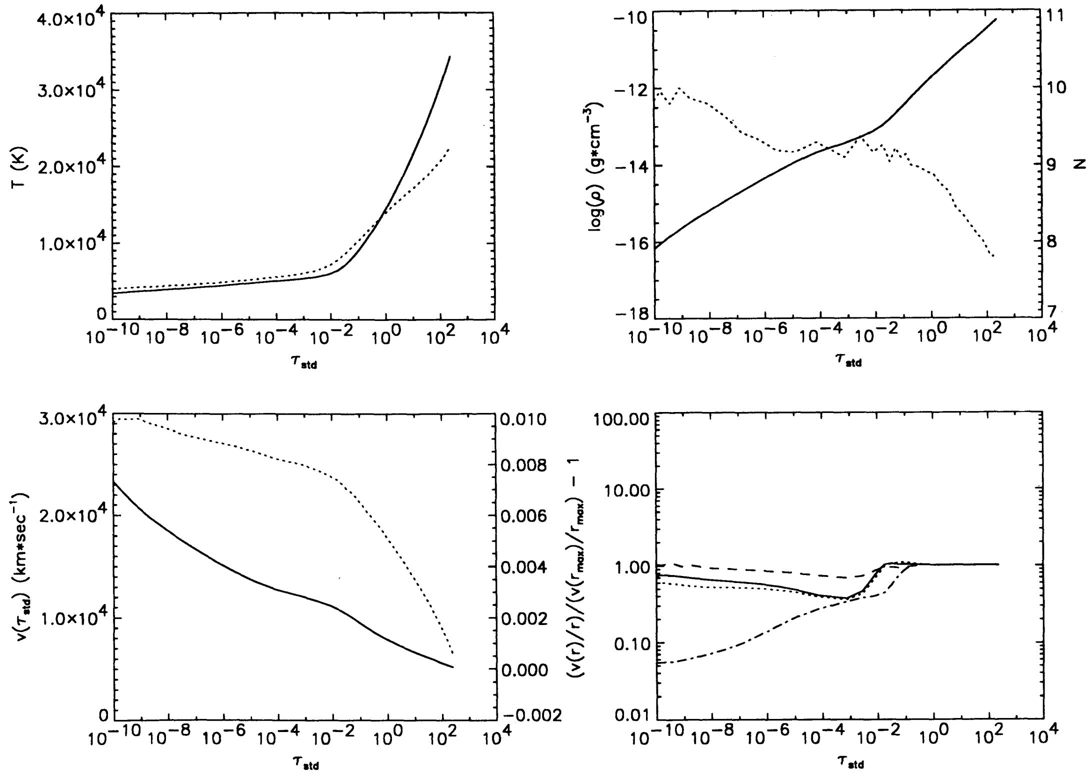
4.0×10^4
3.0×10^4
2.0×10^4
1.0×10^4
0
T (K)
10^-10 10^-8 10^-6 10^-4 10^-2 10^0 10^2 10^4
τ_std
-10
-12
-14
-16
-18
log(ρ) (g*cm^-3)
11
10
9
8
7
N
3.0×10^4
2.0×10^4
1.0×10^4
v(τ_std) (km*sec^-1)
0.010
0.008
0.006
0.004
0.002
0.000
-0.002
(v(r)/r)/(v(r_max)/r_max) - 1
100.00
10.00
1.00
0.10
0.01

FIG. 2d

in a static atmosphere, due to the effects of advection and aberration in a moving medium (cf. Mihalas 1986; Hauschildt 1992b).

Finally, departure coefficients for the ground states of the species treated in non–LTE are shown in Figure 2. Clearly the gas above the photosphere is not in local thermodynamic equilibrium ($b_1 \neq 1$). Early on, during the first two days, the gas is over ionized with respect to LTE. By day 3–4, the b_1's have become smaller than unity due to the fact that the electron temperature in the outer envelope drops much more rapidly than the color temperature of the radiation during the same time interval in the wavelength region most important for the radiative rates of hydrogen. The departures from LTE are not exceptionally large, but they are significant for the line formation process and the ionization equilibrium.

The departure coefficients obtained are very sensitive to the treatment of line blanketing in the UV spectral range. Test calculations in which we artificially neglected line blanketing (but used identical temperature structures) give much smaller b_1's for epochs later than about 0.8 days after the outburst, contrary to the results obtained by Schmutz et al. (1990). The differences are illustrated in Figure 3. For simplicity, we have used the rad-hydro gas temperatures for these test calculations. The results for the RE temperature structures are very similar. The solid curves show the departure coefficients for a model atmosphere in which metal line blanketing by $\sim 10^5$ metal lines is considered; the dotted curves show b_1 in the case of neglected metal line-blanketing. When metal line blanketing is included, b_1 for H I is of the order of 0.1 to 10, depending strongly on the model, while, if line blanketing is neglected, b_1 is of the order of 10^{-4} to 10^{-2}. The differences are caused by the much lower color temperatures for the radiation (the electron temperatures are about the same) in calculations which include line blanketing. The metal lines overlap with the H I Lyman lines and continuum and greatly increase the optical depth of the atmosphere at those wavelengths, in particular in the outer parts of the atmosphere. Therefore, the Lyman and Balmer continua and the Lyman lines become "optically thick" due to the effect of the overlapping metal lines. Line blanketing is equally important, or even more important, in determining the departure coefficients for Mg II and Ca II. This is due to the fact that the resonance lines of these species and their continua are in spectral regions where the Fe II "curtain" dominates the formation of the spectrum (see Hauschildt et al. 1993). The influence is largest at later times, when the temperature is lower and line blanketing is stronger. The departure coefficients are also sensitive to the density structure of the outer photosphere and to the treatment of the metal lines. We plan to investigate these effects in more detail in future studies.

3.3. *Opacities*

As a by-product of calculating spectra, one can also obtain values for various types of mean opacities. As mentioned above, two of the means which appear in the frequency-integrated rad-hydro equations, χ_F and κ_J, cannot be obtained without knowledge of the full spectral distribution of the radiation. Since this information is not typically available when running a gray rad-hydro code, one must use $\chi_{\rm R}$ and $\kappa_{\rm P}$ instead. In Figure 4, we plot the ratios $\kappa_J/\kappa_{\rm P}$ and $\chi_F/\chi_{\rm R}$ (*solid curves*) as functions of optical depth for the SN 1987A snapshots. All means were calculated using the atomic data included in PHOENIX and assumed a statistical velocity of 1000 km s^{-1}. (The statistical velocity is relevant for the Rosseland mean, since it is a harmonic average, but it has no influence on the (arithmetic) Planck mean.) The RE temperature structure calculated by PHOENIX was used, along with the velocity and density structure from VISPHOT. Clearly, κ_J and χ_F are not self-consistent in the sense that, if those means had been used in the rad-hydro model from the beginning, the structure might have evolved somewhat differently, but we can still use these plots to get an idea of how good or bad the assumptions of $\kappa_J = \kappa_{\rm P}$ and $\chi_F = \chi_{\rm R}$ are.

As expected, in optically thick regions, where the radiation field becomes Planckian, κ_J becomes equal to $\kappa_{\rm P}$ and χ_F reduces to $\chi_{\rm R}$. In the optically thin regions of the atmosphere, κ_J can be more than 2–3 times larger than $\kappa_{\rm P}$, the ratio increasing rapidly with decreasing optical depth. Likewise, χ_F can be more than twice as large as the Rosseland mean. The differences between $\kappa_{\rm P}$ and κ_J and between χ_F and $\chi_{\rm R}$ are not huge, but may be significant. Due to the nonlinear nature of the whole evolution of the supernova, the effects of using correct opacities cannot be readily predicted.

The solid lines in Figure 4 show the opacity ratios when all velocity effects are included (case 1), whereas the dotted curves show the ratios for $v(r) = 0$ (case 2). In both cases, the temperature structures and departure coefficients obtained from the full non–LTE radiative equilibrium calculations were used and a statistical velocity of 1000 km s^{-1} was assumed (thus the solution for $v = 0$ is not a true static solution). In case 2, the main effect of setting all velocities to zero was to change the radiation field (J_ν and F_ν) and hence the mean opacities which are integrals over the radiation field.

The velocity affects χ_F more than κ_J as can be seen by examining Figure 4. The dashed curves give the ratios $\kappa_J^{\rm mov}/\kappa_J^{\rm stat}$ (*upper panels*) and $\chi_F^{\rm mov}/\chi_F^{\rm stat}$ (*lower panels*). These ratios indicate the net effect of the velocity field on the mean opacities and, therefore, define an "expansion factor." In Figure 5 we plot the factors separately for several snapshot epochs at once. In general, the expansion factors are not very different from unity even in the outer parts of the envelopes, and they are smaller than the ratios $\kappa_J/\kappa_{\rm P}$ and $\chi_F/\chi_{\rm R}$ themselves. Thus, we conclude that using $\kappa_J^{\rm stat}$ and $\chi_F^{\rm stat}$ rather than $\kappa_{\rm P}$ and $\chi_{\rm R}$ will be nearly as good as using the entirely correct $\kappa_J^{\rm mov}$ and $\chi_F^{\rm mov}$, at least in this simulation at these epochs. This information might be useful in developing a fast subroutine to calculate mean opacities for a rad-hydro code. However, there is a systematic trend clearly seen in Figure 5: The expansion ratios for κ_J are typically smaller than unity, but for χ_F, they are larger than unity (and increase rapidly outward). Although the effect of the expansion on the averaged opacities is relatively small, this systematic effect may have some influence on the time evolution of the expanding shell.

We note that the expansion factors, as we define them here, are completely different from those defined by Karp et al. (1977). Our mean opacities for expanding atmospheres are CMF quantities (the radiation field and the absorption and emission coefficients are all calculated in the frame which is moving with the gas), and both the static and the moving envelopes include line blanketing. In Karp et al. (1977), the expansion factor is obtained by comparing the total *lab frame* opacity for the expanding atmosphere to the electron scattering opacity. For a rad-hydro code (and for traditional diffusion + hydro codes), one needs the *CMF* opacity. The solution of the CMF SSRTE automatically includes the changing Doppler shift of photons relative to the gas they are passing through by means of an $\partial/\partial\lambda$ term, so, in principle, no pro-

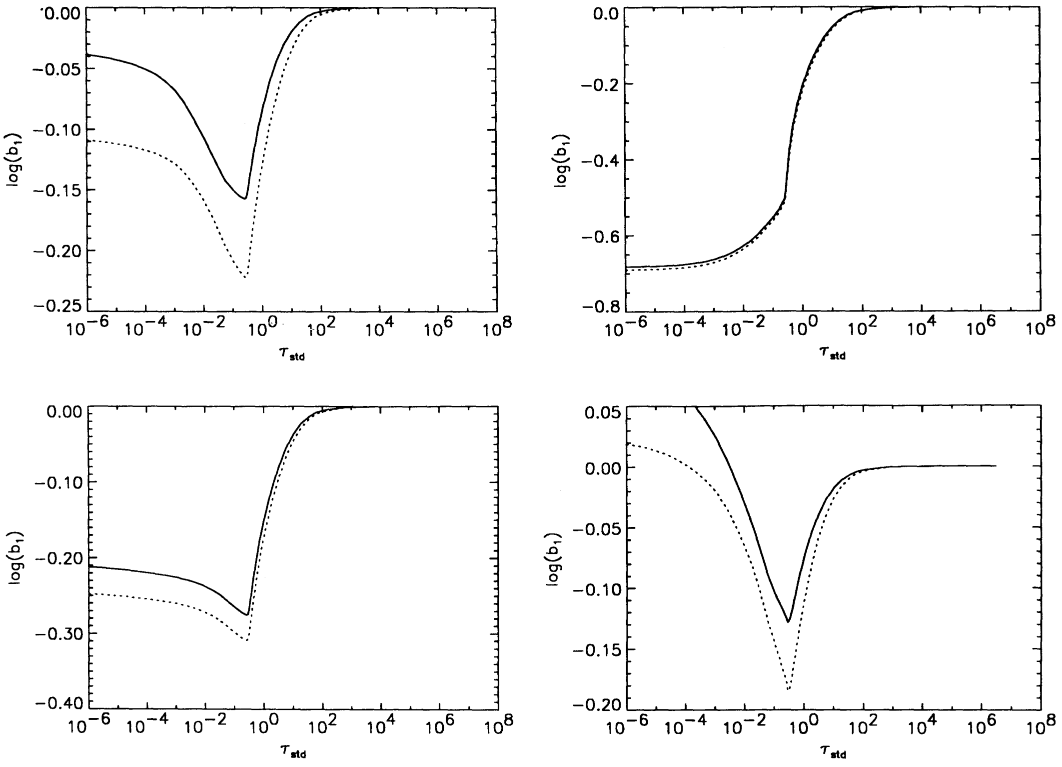

FIG. 3*a*

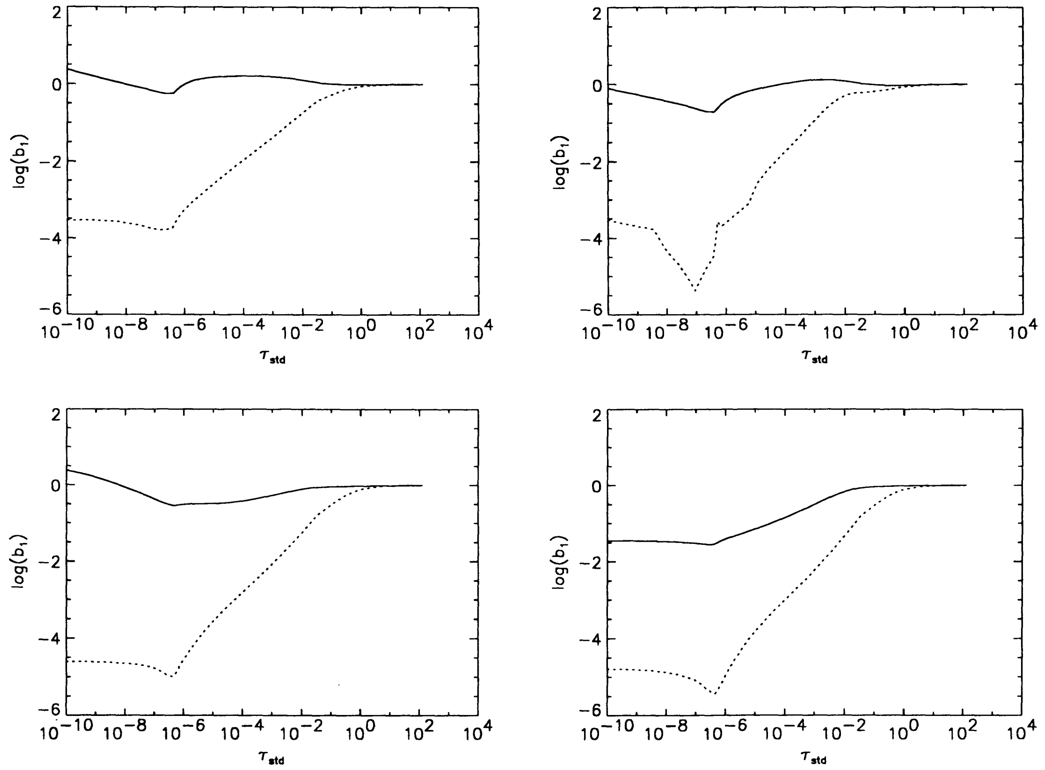

FIG. 3*b*

FIG. 3.—The effect of metal line blanketing on the ground state departure coefficients b_1 for the same epochs shown in Fig. 2. The solid curves give the run of b_1 for a model atmosphere which includes metal line blanketing, whereas the dotted curves show the b_1 for model atmospheres without metal line blanketing. The temperature structure used is the gas temperature obtained by the rad-hydro simulation. The term "metal line blanketing" means, in this context, the effects of lines other than the included non–LTE lines on the radiation field and radiative rates. Background LTE continuum absorption is included in all cases; *upper left*, H I; *upper right*, He I.

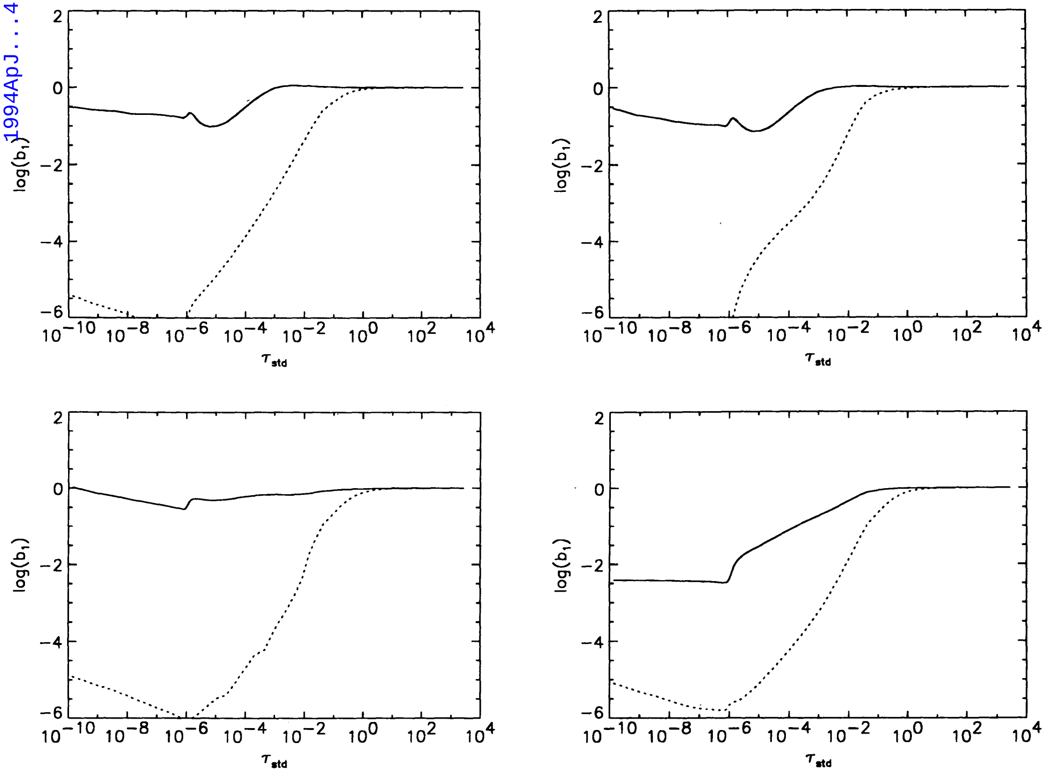
log(b₁)
2
0
−2
−4
−6
10⁻¹⁰ 10⁻⁸ 10⁻⁶ 10⁻⁴ 10⁻² 10⁰ 10² 10⁴
τstd

FIG. 3*c*

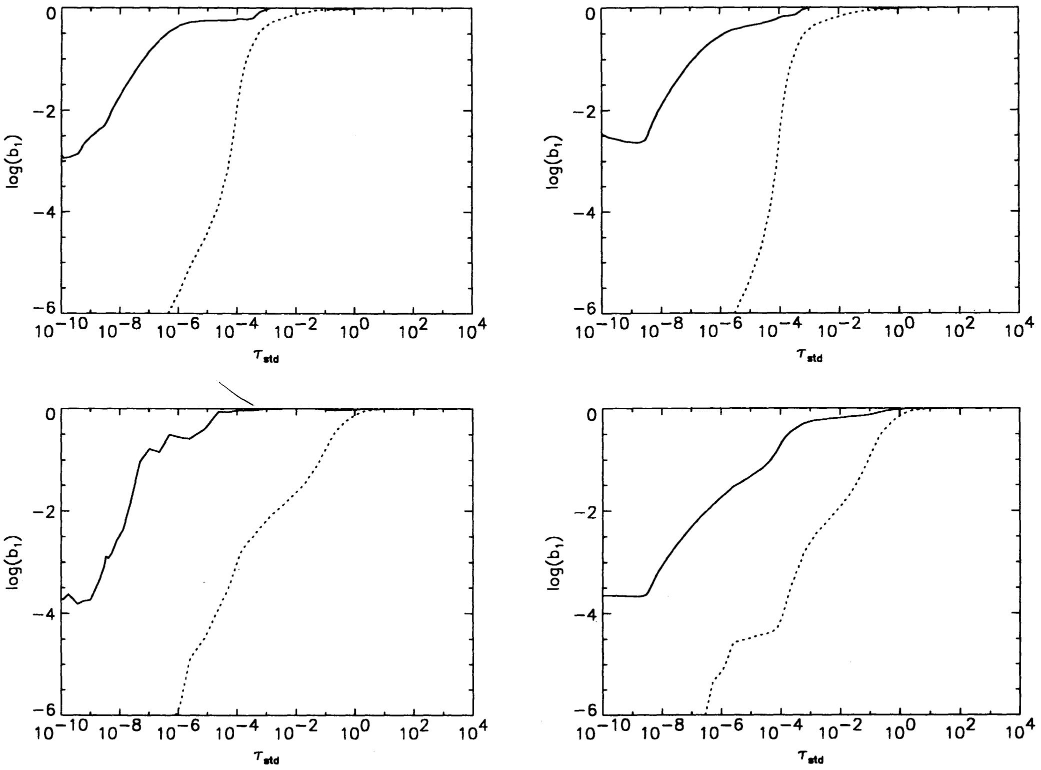
log(b₁)
0
−2
−4
−6
10⁻¹⁰ 10⁻⁸ 10⁻⁶ 10⁻⁴ 10⁻² 10⁰ 10² 10⁴
τstd

FIG. 3*d*

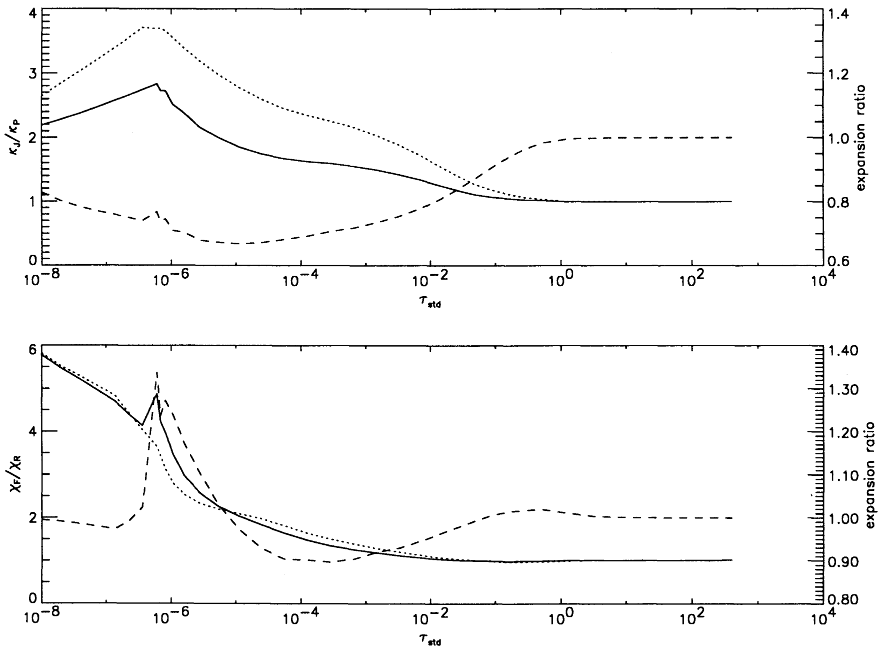

FIG. 4*a*

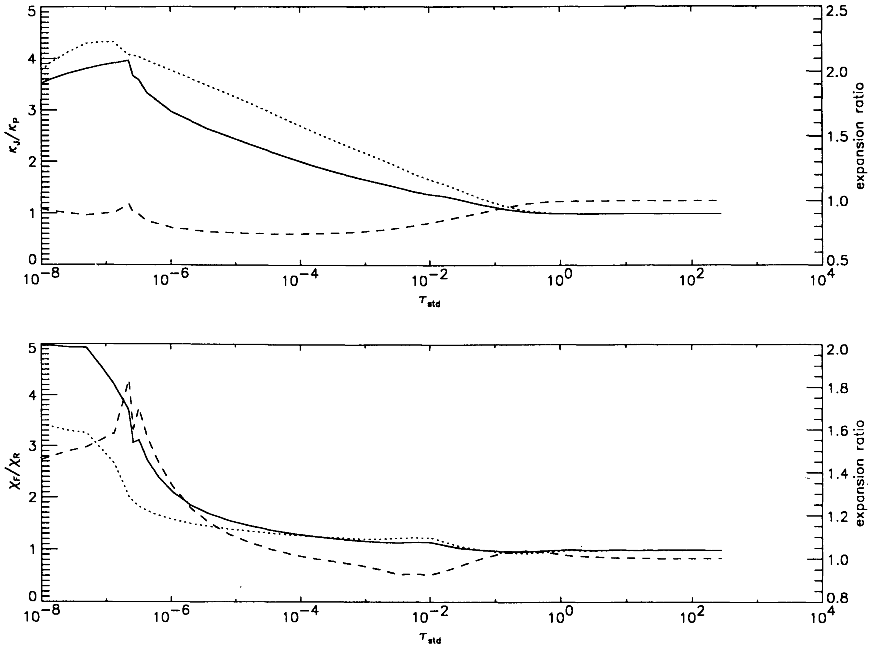

FIG. 4*b*

FIG. 4.—The ratios κ_J/κ_P and χ_F/χ_R as functions of standard optical depth for snapshot model atmospheres at $t = 0.73$ day (*a*), 1.26 day (*b*), 2.09 day (*c*), and 3.85 day (*d*) after core collapse. The full curves show the results for atmosphere models including the effects of the velocity field on the radiation, whereas the dotted curves show the results obtained by neglecting the velocity field. In addition, the dashed curve shows the "expansion ratios" $\kappa_J^{\rm mov}/\kappa_J^{\rm stat}$ (*upper panels*) and $\chi_F^{\rm mov}/\chi_F^{\rm stat}$ (*lower panels*) with the scale on the right-hand side. The temperature structures and the departure coefficients were taken from RE solutions, velocity terms included, in all cases.

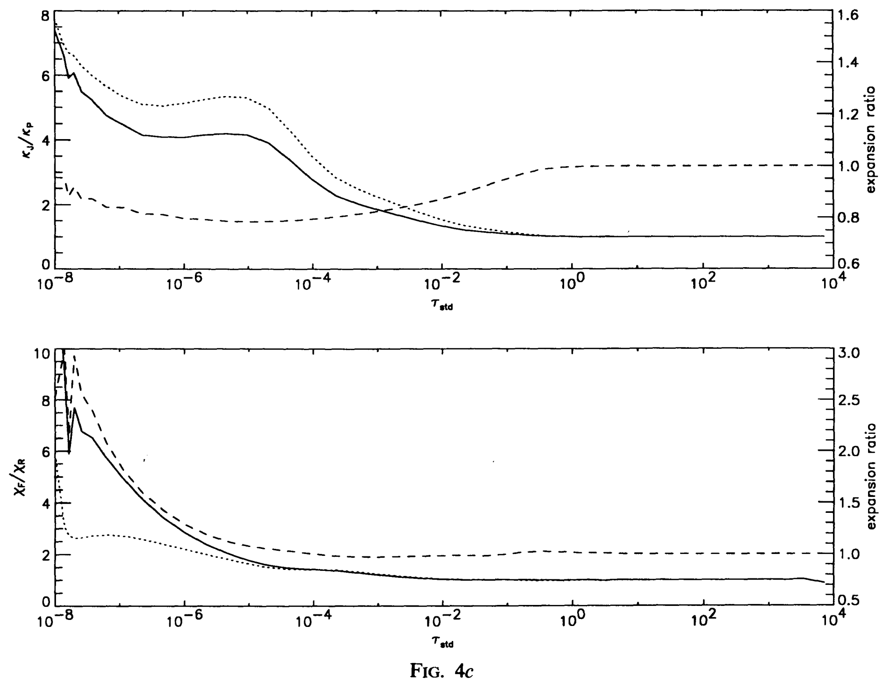

FIG. 4c

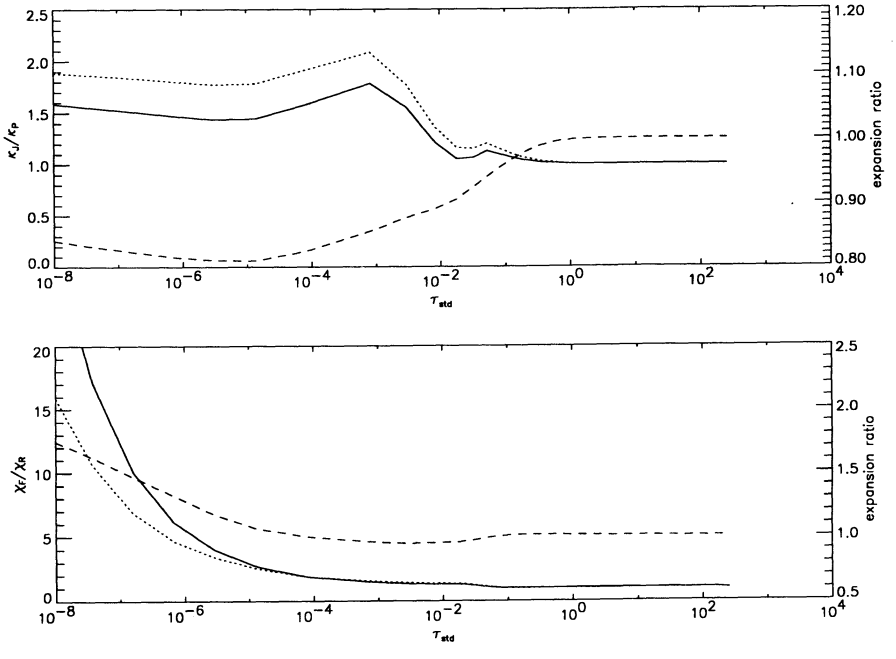

FIG. 4d

cedure such as is derived in Karp et al. (1977) is necessary. Advection and aberration terms are also included. Accordingly, the primary difference between the Eulerian frame and the Lagrangian frame pictures for the mean opacities is that in the Eulerian frame picture the specific intensities as well as the monochromatic opacities are changed by the velocity field, whereas in the Lagrangian frame picture only the specific intensities are changed.

Furthermore, since the total extinction is compared to only the electron scattering opacity in Karp et al. (1977), one cannot tell from their expansion factor how much of the opacity enhancement is due to the velocity gradient and how much is simply due to including lines. Even in the static case, including line blanketing would give a large opacity enhancement. The expansion factors we define here can be both larger and smaller than unity, depending on the details of the radiation field as a function of optical depth. For example, the presence of emission lines in very early stages of the SN outburst (and in nova atmospheres) may produce very different expansion factors. We plan to investigate the systematic behavior of the expansion factor, as well as the influence of the assumed statistical velocity, in more detail in further studies.

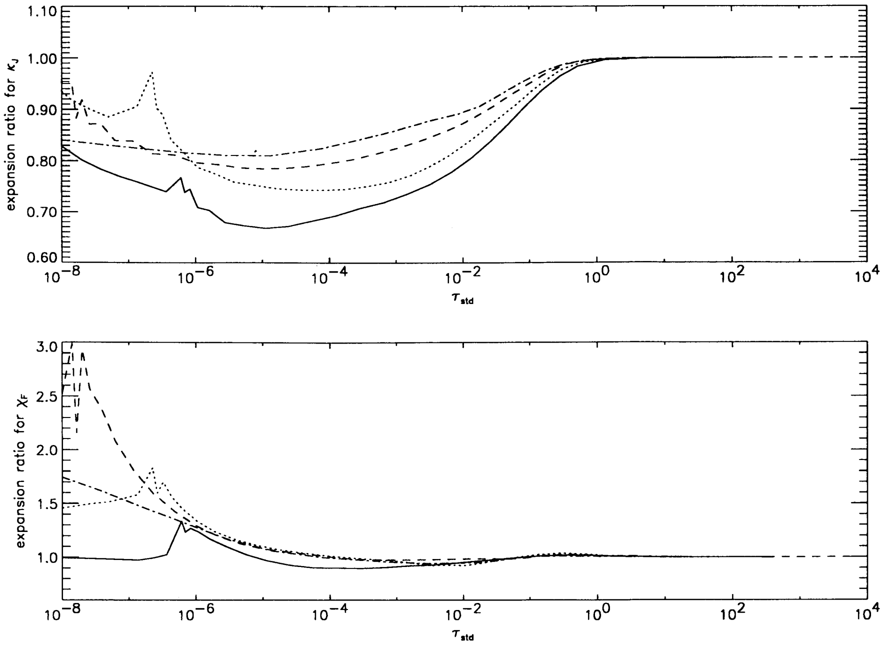

FIG. 5.—The ratios $\kappa_J^{\rm mov}/\kappa_J^{\rm stat}$ (*upper panel*) and $\chi_F^{\rm mov}/\chi_F^{\rm stat}$ (*lower panel*) as functions of optical depth for the epochs $t = 0.73$ day (*solid curves*), 1.26 day (*dotted durves*), 2.09 day (*dashed curves*), and 3.85 day (*dash-dotted curves*) after core collapse. The temperature structures and the run of the departure coefficients for the model atmospheres were taken from the corresponding RE snapshot models.

3.4. *Synthetic Spectra*

Figure 6 shows two series of synthetic spectra from the UV through the near-infrared. Panel (*a*) shows spectra computed using the rad-hydro temperature structure $T_{\rm gas}(r)$, whereas panel (*b*) displays the spectra calculated using the radiative equilibrium temperature structure $T_{\rm RE}$. The flux scales are logarithmic and the spectra are shifted by 0.5 dex relative to each other. The strong time dependence of the early spectra, i.e., during the first 2 days, is very prominent. After about 2 days, the spectral evolution slows down somewhat.

The topmost two spectra in Figure 6*a* and the topmost spectrum in Figure 6*b* are dominated by the Al III resonance lines at 1856 Å and the Mg II $h + k$ lines at 2800 Å. The latter blend possesses a pronounced P Cygni profile in the earliest spectra. Note the huge Doppler shifts of the absorption components (about 16,000 km $\rm s^{-1}$ for Al III and 20,000 km $\rm s^{-1}$ for Mg II). The Balmer lines of H I are relatively weak, as is He I 5876 Å. The Ca II H + K lines and the Ca II infrared triplet are not visible in the synthetic spectra for the first two days. The situation changes in the subsequent spectra. Once the SN has cooled sufficiently, the Ca II H + K λ3934, 3969 Å lines form the most prominent absorption feature in the near-UV, and the Balmer lines of H I become the strongest features in the optical region. In the infrared, the Ca II triplet 8435, 8544, 8597 Å appears first as an absorption feature, but at later times, an emission component develops and the feature attains a P Cygni profile.

The differences between the two sets of synthetic spectra are largest at early times (1–2 days after core collapse), when differences between RE and rad-hydro temperature structures are greatest. The effects are particularly striking in the UV which is the most temperature-sensitive wavelength region. Because temperatures in the ejecta fall smoothly with time, differences between $T_{\rm gas}(r)$ and $T_{\rm RE}(r)$ are basically equivalent to a shift in time. In other words, a RE spectrum computed for a snapshot model atmosphere at epoch t_1 appears very similar to a synthetic spectrum computed using $T_{\rm gas}(r)$ at an earlier time t_2.

In Figure 7 we directly compare synthetic spectra computed using the RE temperature structure (*full curves*) with spectra computed using "earlier" rad-hydro temperature structures (*dotted curves*, shifted by +1 dex). The non–LTE rate equations were iterated to full convergence in both cases, so that each synthetic spectrum is self-consistent for the given temperature structure. The upper panel of Figure 7 shows spectra for the epochs $t_{\rm RE} = 1.26$ day and $t_{\rm gas} = 0.73$ day, the middle panel spectra for $t_{\rm RE} = 2.09$ day and $t_{\rm gas} = 1.26$ day, and the lower panel synthetic spectra for $t_{\rm RE} = 3.85$ day and $t_{\rm gas} = 3.24$ day. (Even closer correspondences could presumably have been found if we had available a large enough collection of snapshots, particularly for early times.) For epochs later than those shown, the "time shifts" needed to match the spectra are smaller, because the temperatures change more slowly. The similarity of the pairs of spectra show the importance of the temperature structure in determining the appearance of the spectrum at early times. However, differences of up to several thousand km $\rm s^{-1}$ in the wavelength shifts of strong lines occur due to differences in the location of the photosphere and the line-forming region in velocity space (see also Figs. 8, 9, and 10).

3.5. *Comparison to SN 1987A*

Figure 8 shows a comparison between the 1987 February 25, *IUE* and optical spectra of SN 1987A ($\approx$1.5 day after core collapse) and synthetic spectra for two snapshot model atmospheres. The synthetic spectra are at the epochs $t = 1.26$ day for $T(r) = T_{\rm gas}(r)$ and $t = 2.09$ day for $T(r) = T_{\rm RE}(r)$. The different epochs used for the synthetic spectra are a consequence of the different temperature structures obtained by the rad-hydro

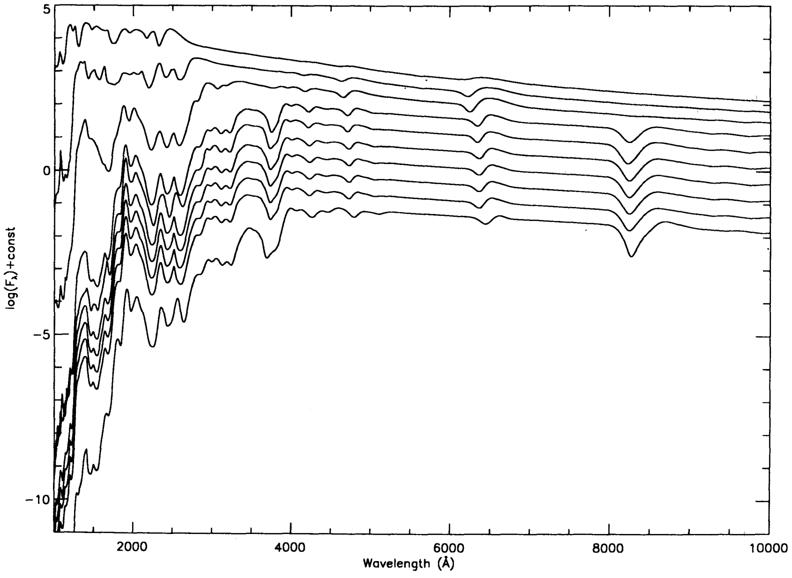

FIG. 6*a*

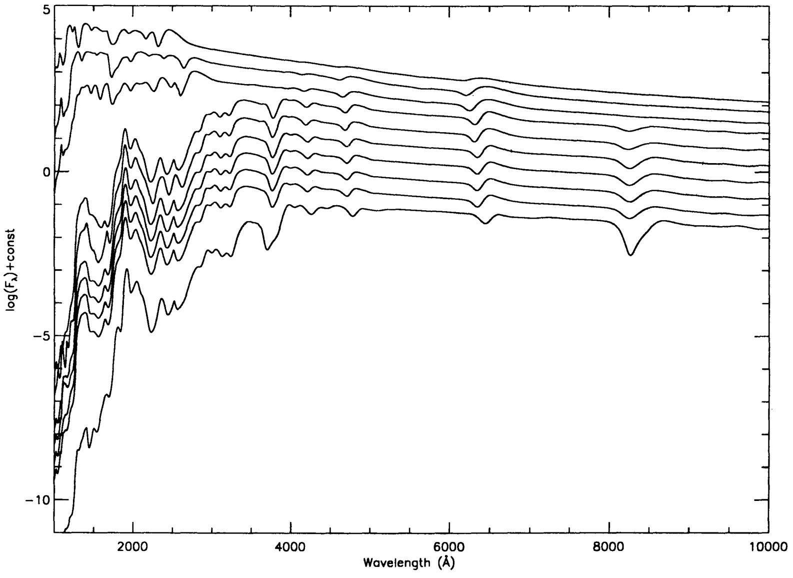

FIG. 6*b*

FIG. 6.—Non–LTE synthetic spectra for different rad-hydro snapshot structures. The first panel (*a*) shows spectra calculated using the $T_{\rm gas}$ structure taken from the rad-hydro simulation; the second plot (*b*) shows spectra derived from the corresponding non–LTE radiative equilibrium temperature structure. All atmospheric models include non–LTE effects self-consistently with line blanketing by about 10^5 metal lines. The epochs for the snapshot models range from $t = 2.45$ hr (*topmost spectrum*) to ≈ 4 day after core collapse. The spectra have been shifted by ~ 0.5 dex relative to each other for clarity.

simulation and the model atmosphere RE calculation as discussed in the previous section. In Figure 8 and subsequent figures discussed in this section, the full curves show the observed spectra, the dotted curves the synthetic spectra computed using $T(r) = T_{\rm gas}(r)$, and the dashed curves the synthetic spectra computed using the radiative equilibrium temperature structure $T(r) = T_{\rm RE}(r)$. All observed spectra have been dereddened using the LMC reddening law and a color excess of $E(B-V) = 0.18$. The optical data have been taken from Phillips et al. (1987).

As shown in Figure 8 (*upper panel*), the UV spectrum is, overall, reproduced well by both synthetic spectra, although the flux in the models is too high between 2300 and 2600 Å. The Mg II $h + k$ doublet emission feature (at $\sim$2800 Å) is matched well, but the absorption component on the blue side shows a slightly too small width in the synthetic spectra. The blend of the Al III 1856 Å resonance lines with the Si II 1808, 1810 Å doublet at an observed wavelength of $\sim$1700 Å is slightly too broad, and the absorption features between 1400 and 1600 Å, due to C IV 1550 Å, Si II 1533 Å, and Si II 1400 Å, are not formed at high enough velocity. The "emission" feature seen in the RE synthetic spectrum originates from a very temperature sensitive gap in the "iron curtain" due to overlapping lines of carbon, oxygen, and iron.

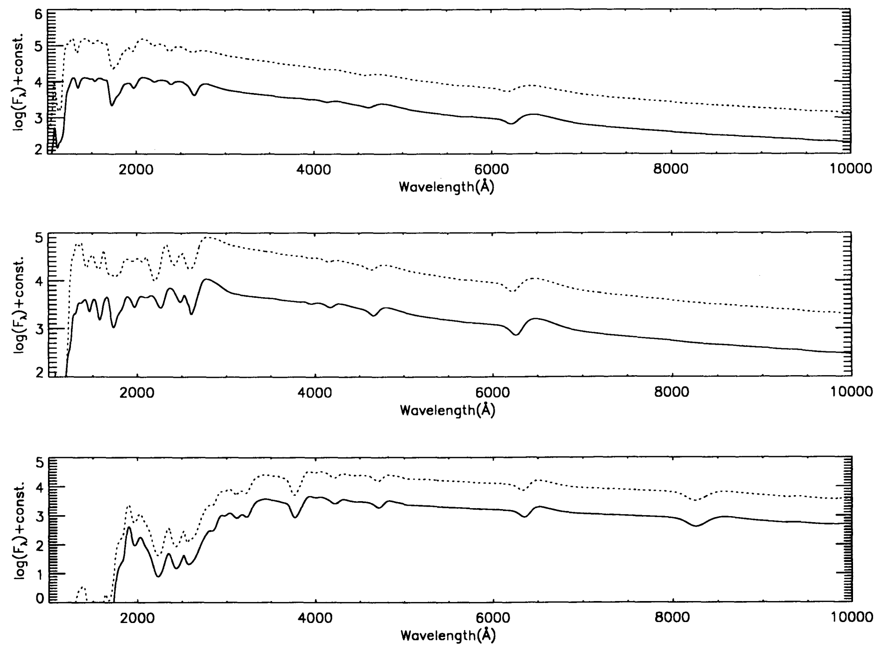

FIG. 7.—A comparison between synthetic spectra calculated using the assumption of radiative equilibrium in the Lagrangian frame (*full curves*) and using the gas temperatures provided by the rad-hydro simulation (*dotted curves*). For both model atmosphere sequences we have solved the non–LTE radiative transfer and rate equations consistently with the specified temperature structure. The upper panel shows the synthetic spectra for the epochs $t_{\rm RE} = 1.26$ day and $t_{\rm gas} = 0.73$ day, the middle panel spectra for $t_{\rm RE} = 2.09$ day and $t_{\rm gas} = 1.26$ day, and the lower panel synthetic spectra for $t_{\rm RE} = 3.85$ day and $t_{\rm gas} = 3.24$ day, where $t_{\rm RE}$ and $t_{\rm gas}$ denote the epochs for model atmospheres computed using $T(r) = T_{\rm RE}(r)$ and $T(r) = T_{\rm gas}(r)$, respectively.

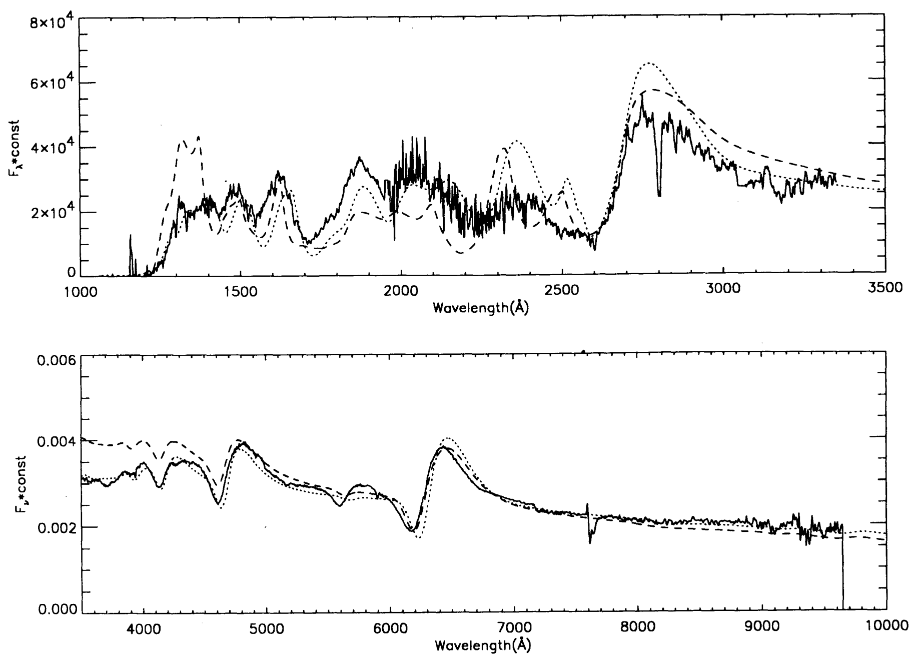

FIG. 8.—Comparison of the observed UV and optical spectra of SN 1987A on 1987 February 25 with synthetic spectra. The full curves give the observed spectrum, whereas the dotted curves give the synthetic spectrum computed using a Lagrangian radiative equilibrium temperature structure at $t = 2.09$ day after core-collapse and the dashed curves the synthetic spectra obtained using the gas temperature structure of the rad-hydro simulation at $t = 1.26$ day after core collapse.

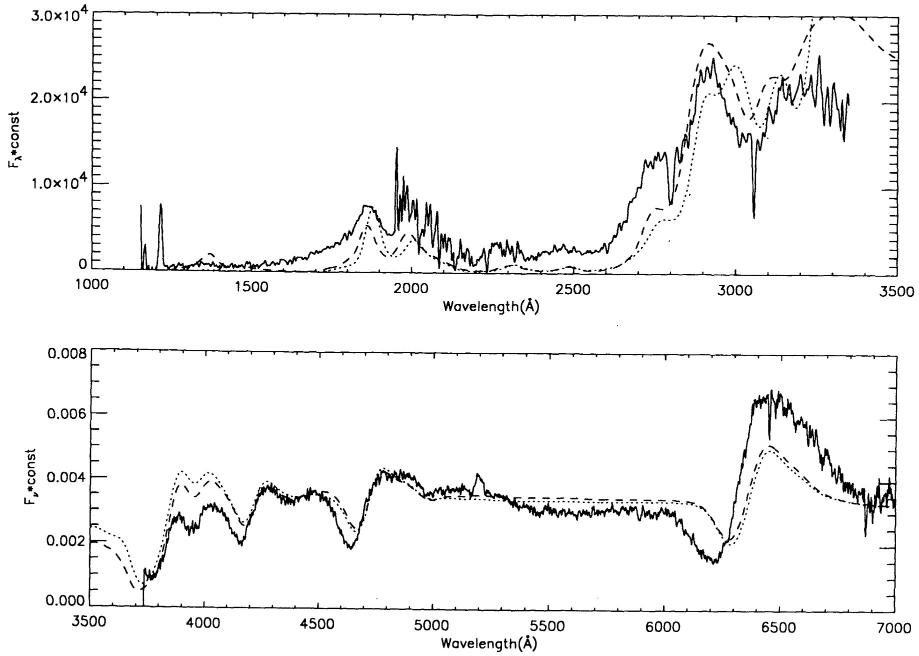

FIG. 9.—The upper panel shows the observed UV spectrum of SN 1987A on 1987 February 26 (*full curve*) and the synthetic spectra for the epochs $t = 3.49$ day [*dotted curve*, using $T(r) = T_{\rm RE}(r)$] and 2.09 day [dashed curve, using $T(r) = T_{\rm gas}(r)$]. The lower panel shows the optical spectrum of SN 1987A at 1987 February 27 (*full curve*) and the synthetic spectra for the epochs $t = 3.49$ day [*dotted curve*, using $T(r) = T_{\rm RE}(r)$] and 2.09 day [*dashed curve*, using $T(r) = T_{\rm gas}(r)$].

In the optical continuum above 4000 Å (Fig. 8 *lower panel*), the agreement between theory and observation is also quite good, for both synthetic spectra. Below 4000 Å the errors in the reddening correction and the flux calibration are largest, so the deviations from the observed spectrum are to be expected. The model atmosphere reproduces the profile of the Balmer lines of H I remarkably well. However, the He I 5876 Å line is much too weak and at too low a velocity in both synthetic spectra.

In general, we can say that the model atmosphere is able to reproduce the observed spectrum well. Although the expansion velocity in the line-forming region seems to be slightly too low for some lines, the velocity gradient, which influences the widths of the lines, gives good results. The density structure at this early stage of the outburst seems to be quite well modeled by the rad-hydro model. We think that a better fit could be obtained by choosing a slightly different epoch for the rad-

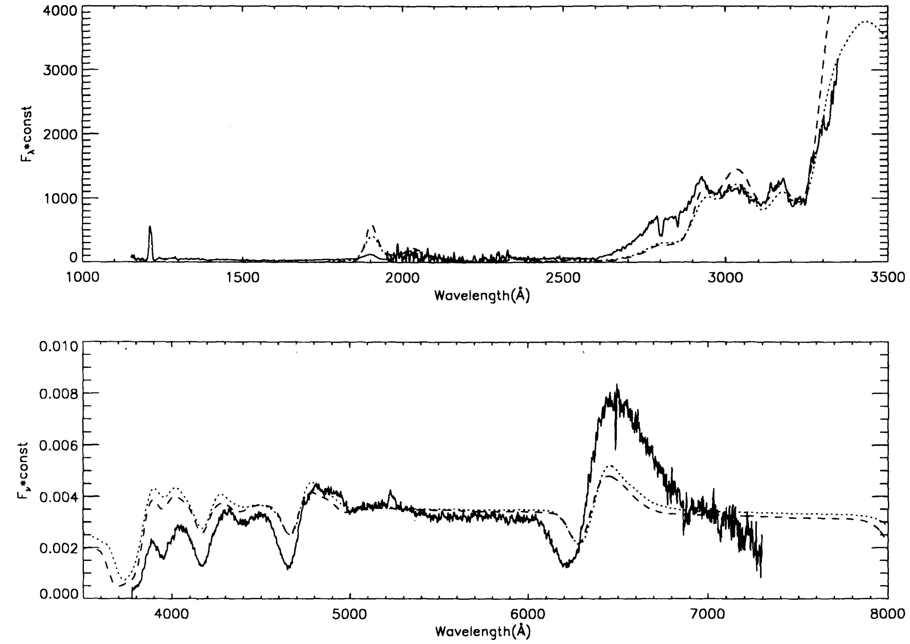

FIG. 10.—The upper panel shows the observed UV spectrum of SN 1987A on 1987 March 1 (*full curve*) and the synthetic spectra for the epochs $t = 3.85$ day [*dotted curve*, using $T(r) = T_{\rm RE}(r)$] and 3.85 day [*dashed curve*, using $T(r) = T_{\rm gas}(r)$]. The lower panel shows the optical spectrum of SN 1987A at 1987 February 28 (*full curve*) and the synthetic spectra for the epochs $t = 3.85$ day [*dotted curve*, using $T(r) = T_{\rm RE}(r)$] and 3.85 day [*dashed curve*, using $T(r) = T_{\rm gas}(r)$].

1994ApJ...424..905H

hydro model since, at this early phase, the synthetic spectra are very sensitive to the epoch. However, obtaining an optimum fit is not our goal in this paper; rather we wish to investigate physical effects and approximations and demonstrate the ability of our approach to generally reproduce spectra and light curves of SNs.

In Figure 9 we compare the observed UV and optical spectra of February 26 and 27 (days ≈2.5 and ≈3.5, respectively) to snapshot models at the epochs $t = 2.09$ day [for $T_{\rm gas}(r)$] and $t = 3.49$ day [for $T_{\rm RE}(r)$]. The spectrum has changed significantly, now showing a much "cooler" appearance with relatively few features in the UV. The Mg II $h + k$ emission has disappeared due to the lower temperatures at this epoch; only a small plateau around 2800 Å and the deep absorption just blueward of the plateau indicate the presence of the doublet. The broad dip at ~3000 Å and the "emission" feature at 1800–2050 Å with an embedded "absorption line" are both reproduced in the synthetic spectra. These features are sculpted by variations in the density of many strong absorption lines of Fe II, Cr II, and Ti II. The "emission" features occur at gaps in this "iron curtain" (e.g., at ~2900 Å). Althouth differences between the radiative equilibrium model and the rad-hydro model are small, variations in the spectrum are relatively large, indicating that these features are very sensitive to the temperature structure of the model (see especially the region beyond 3200 Å.)

In the optical spectral range, the agreement between synthetic and observed spectra is perhaps slightly better than in the UV. The slope of the continuum is very well reproduced by the synthetic spectrum above 4200 Å. Below 4200 Å the observed spectrum declines somewhat faster than the model spectrum; however, the general shapes of Hγ and Hδ are very similar to the observed profiles. Hα is too weak and the absorption component is at too low a velocity in the synthetic spectrum. Hβ has the correct flux but is also at a slightly too small velocity.

In Figure 10 we compare the synthetic spectra for $t = 3.86$ day with the slightly later *IUE* and optical spectra of SN 1987A of 1987 March 1 and February 28 (days ≈5.0 and ≈4.5). The synthetic spectra reproduce the plateau visible in the UV spectrum between 2900 and 3300 Å, as well as the rapid flux increase above 3300 Å. The structure of the plateau is also reproduced, although the features in both synthetic spectra are slightly too broad. The flux drops rapidly below 2800 Å, with the exception of two small emission features at about 1900 Å. Both features are reproduced by the synthetic spectra though the flux of the bluer one is too high.

The fit to the optical spectrum of 1987 February 28, is not as good as the fit to the nearly simultaneous *IUE* spectrum. The synthetic spectrum reproduces the excess emission of Hα, although the line is too weak by about a factor of 2 in the emission part and by about 20% in the absorption part. The velocity is also significantly too low. Hβ, Hγ, and Hδ are at the correct blueshift, but their absorption components are too weak in the synthetic spectra. These discrepancies may be caused by relatively small differences between the theoretical and the actual SN 1987A density structures. The rad-hydro density profile for this epoch is, in the region of the formation of the Hα line, close to a power law $\rho \propto r^{-N}$ with $N \approx 9$. A lower N could lead to a relative increase in the emission (Schmutz et al. 1990). The differences between observed and predicted Doppler shifts of the Balmer lines could be explained by a somewhat higher luminosity than used in our calculation. This would increase the temperature in the outer layers of the photosphere and move the optical line-forming region outward into higher velocity material, increasing the velocities (and strengths) of the Balmer lines.

In general, the agreement between observed and synthetic spectra is remarkably good, particularly in view of the fact that we have not fine tuned the fit by, e.g., matching the epoch better or altering the abundances.

3.6. *The Early Light Curve and Color Indices of SN 1987A*

Using the synthetic spectra calculated for several rad-hydro epochs, we can derive the early light curve of SN 1987A in various broad-band colors. For this purpose, we have used the synthetic spectra calculated using the rad-hydro temperature structures, $T(r) = T_{\rm gas}(r)$, to circumvent the "time-shift" problems created by using $T(r) = T_{\rm RE}(r)$ (see § 3.4). Theoretical Johnson *UBVR* and *I* light curves are calculated for the first 5 days of the outburst using the code of Allard (1993); the results are displayed in Figure 11. The plus symbols are the observed magnitudes (Phillips et al. 1988), whereas the solid lines give the theoretical light curves in the different bandpasses. The synthetic spectra have been reddened by $E(B-V) = 0.18$ to account for the reddening of the observed colors. In Figure 12 we compare the observed $(U-B)$, $(B-V)$, $(V-R)$, and $(R-I)$ color indices (*plus symbols*) with the theoretical color indices (*full curves*). The agreement between theory and observation is

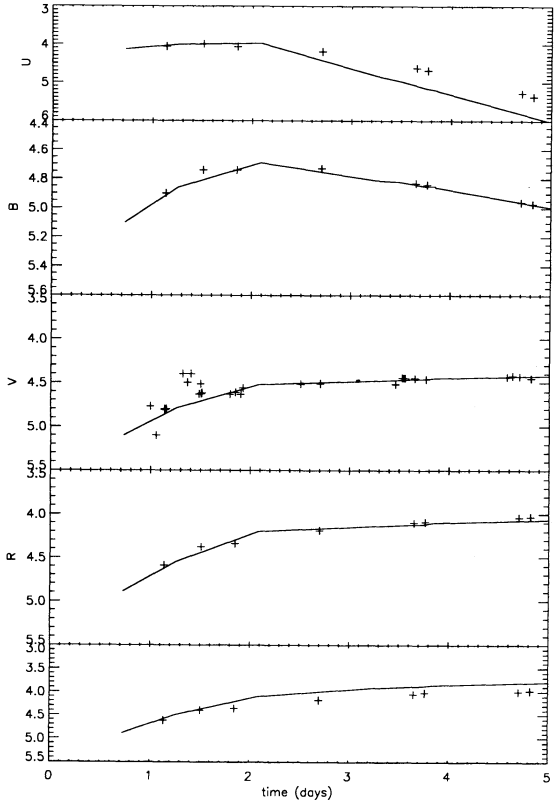

FIG. 11.—The early light curves of SN 1987A in Johnson's *UBVRI* colors (topmost to bottom panels, plus symbols, Catchpole et al. 1987) are compared to theoretical colors (*full curves*). The colors were computed using the model atmosphere for $T(r) = T_{\rm gas}(r)$ in order to be consistent with the bolometric light curve shown in Fig. 1. The synthetic spectra were reddened using $E(B-V) = 0.1$ before computing the colors, which were normalized to an A0 V star.

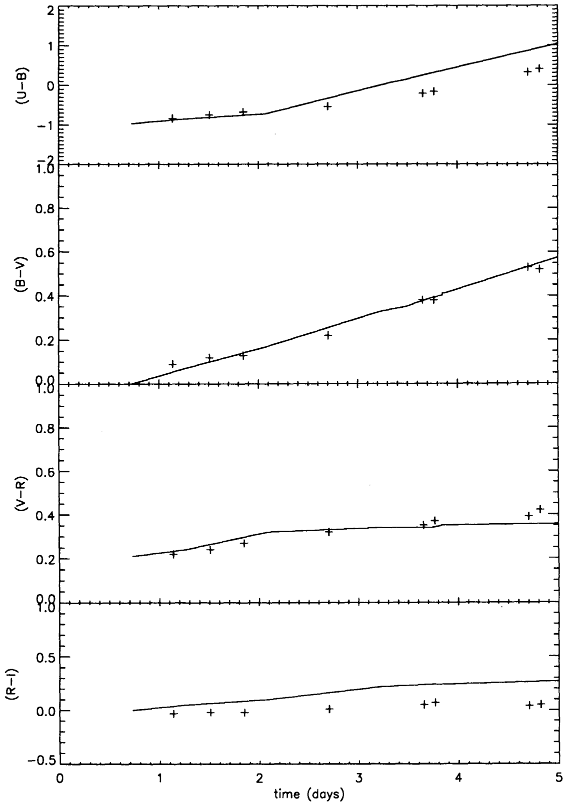

FIG. 12.—As Fig. 11 but for the color indices $(U-B)$, $(B-V)$, $(V-R)$, and $(R-I)$ (*top to bottom panels*, respectively).

remarkably good for V, B, and R, and consequently for $(B-V)$ and $(V-R)$, at all epochs considered here. The results for U and I, and $(U-B)$ and $(R-I)$, are not as good. The U-band light curve of the theoretical calculation declines somewhat too steeply after about 2 days into the outburst. This could be caused by deviations from the assumed reddening and/or by a too rapid cooling of the outer regions of the envelope. The theoretical I light curve, on the other hand, rises a little too quickly, but the effect is small. It could be caused by the way the colors are calculated: In the observation, the normalization is done by comparison to standard stars, whereas the theoretical colors are normalized to the theoretical energy distribution of an A0 V star. For the extended atmospheres found in SNs, this can lead to significant systematic differences between the normalization of the short-wavelength bands, e.g., the U band, and the long-wavelength bands, e.g., the I band, due to the different shapes of the energy distributions of the standard stars and the SN.

4. SUMMARY AND DISCUSSION

In this paper, we have modeled the early evolution of SN 1987A, as a particular application, in order to study various fundamental issues important in the modeling of SN light curves and spectra. The hydrodynamics and bolometric light curve were obtained by solving the spherically symmetric, $O(v/c)$, CMF, frequency-integrated equations of radiation-hydrodynamics (Mihalas & Mihalas 1984). These equations include energy and momentum exchange between the gas and the radiation field and are not limited by the assumptions of one-temperature radiative diffusion. The model atmospheres included non–LTE effects of H I, He I, Mg II, and Ca II and line blanketing by about 10^5 metal lines (mostly due to Fe II multiplets). They were calculated by solving, self-consistently, the spherically symmetric, time-independent, special relativistic equation of radiative transfer and the rate equations for the non–LTE species, assuming density and velocity structures obtained from the rad-hydro simulation. The temperature structures were taken from either the rad-hydro simulation or computed using the assumption of special relativistic RE in the CMF.

We have found that our model for SN 1987A is able to reproduce the observed optical and UV spectra, as well as the light curve (bolometric, U, B, V, R, and I) quite well overall. The differences between the observed and computed spectra are small for the first 2 days after the explosion and are somewhat larger at later stages. In particular, the Balmer lines in our models are too weak and their velocities are too small (by ~ 1000 km s^{-1}) for epochs later than about 3 days. Following Schmutz et al. (1990), we attribute these discrepancies to differences between the density structure of SN 1987A and the density structure obtained by the rad-hydro simulation. The density gradient in the outer part of the envelope is apparently slightly too flat in the model. The UV spectra are reproduced very well, however. For example, the strong Mg II $h+k$ lines which are prominent in the observed spectrum of 1987 February 25, are well reproduced by the models. We believe that a fine-tuning of the parameters of the simulation (e.g., the progenitor structure, the explosion energy, and/or the abundances) may improve the fits even more, but we have decided to defer such an exercise in order to concentrate on basic physical effects.

One common assumption made in general supernova spectrum modeling is that of homologous expansion. For SN 1987A, we have found that the velocity structure is *not* homologous for approximately the first day and a half of the outburst. The deviations from a linear velocity law can amount to 10% in the line-forming region, which is significant for the formation of the early SN spectrum. However, the velocity field becomes homologous very quickly as the ejecta expands. It would be extremely valuable to obtain observations of other SNs at very early stages to check the predictions for the velocity evolution made by rad-hydro simulations.

Radiative equilibrium is another common assumption in spectral modeling. In the models presented here, we find important differences between the temperature structures obtained from the rad-hydro simulation and those obtained from the spectrum code under the assumption of radiative equilibrium. In the outer, optically thin parts of the envelope ($\tau_{\rm std} \leq 0.1$), the RE temperatures are higher than the temperatures obtained in the rad-hydro simulation. However, the gradient of $T_{\rm gas}(r)$ corresponds with a good accuracy to the temperature gradient of a model atmosphere in RE. The offset in absolute value may be due to differences in the opacities used or the treatment of the radiation (gray vs. multifrequency). In the inner, very optically thick parts of the envelope, the RE temperatures are much lower than the gas temperatures of the rad-hydro simulation. This is caused by energy exchange between the *moving* material and the radiation field. Clearly the deeper parts of the envelope are not in strict RE. However, these layers are too optically thick to have a significant influence on the continuum or line spectrum. We conclude that the assumption of RE is a useful approximation for spectral synthesis purposes (at least after the extremely brief period of shock breakout).

We have also found that departures from LTE are significant for the formation of the spectrum during this early phase of the SN evolution (though not for the energy balance), and that the degree of departure from LTE is sensitive to metal line blanketing in the UV for epochs later than about 0.5 days (after the envelope has cooled to an effective temperature less than $\sim 15,000$ K). Line blanketing affects the departure coefficients by increasing the optical depth in the outer parts of the envelope in both the non–LTE continua and line transitions.

An important by-product of our model atmospheres calculations is the ability to compute various mean opacities which appear in the rad-hydro equations. Computation of κ_J and χ_F require knowledge of the full spectral distribution of the radiation field. We find that in the outer regions of the envelope ($\tau_{\rm std} \le 10^{-1}$), the ratios $\kappa_J/\kappa_{\rm P}$ and $\chi_F/\chi_{\rm R}$ are larger then unity and increase rapidly with decreasing $\tau_{\rm std}$. The effects of the velocity field on the opacity averages are, in comparison, small. We find that the "expansion factors," which we have defined as $\kappa_J^{\rm mov}/\kappa_J^{\rm stat}$ and $\chi_F^{\rm mov}/\chi_F^{\rm stat}$, are close to unity in most parts of the envelope. However, $\kappa_J^{\rm mov}/\kappa_J^{\rm stat}$ is typically smaller than unity, whereas $\chi_F^{\rm mov}/\chi_F^{\rm stat}$ is typically larger than unity. This systematic effect could lead to differences in the time evolution of the expanding shell. Note that the "expansion factors" as we define and use them here are very different from the "expansion opacity" defined in Karp et al. (1977). Clearly, this topic has to be considered in more detail in subsequent investigations.

As the next step in this project we will investigate the influence of the opacities on the light curves, temperature structures, and hydrodynamics of type II SNs. Tables for $\kappa_{\rm P}$ and $\chi_{\rm R}$ are then computed by an equation of state and opacity routine derived directly from the stellar atmospheres code used to subsequently calculate the spectra (Ensman et al. 1993). This has the advantages of allowing $\kappa_{\rm P}$ to exceed $\chi_{\rm R}$ (in contrast to the formula for $\kappa_{\rm P}$ which we were forced to use for the rad-hydro models in this paper), permitting the inclusion of molecular opacity sources, and enabling various assumptions about the degree of line scattering to be made. As far as we are aware, molecular opacity has never been included in light curve models, although it is important at late epochs when the ejecta have cooled to $T_{\rm gas} < 3000$ K. Furthermore, use of customized tables ensures that the mean opacities used for the rad-hydro are consistent with the abundances and the atomic physics used for the spectral synthesis. We will also focus on increasing our understanding of the meaning of certain secondary quantities derived from rad-hydro codes, such as the location of the thermalization depth and the color temperature of the emitted radiation.

We thank F. Allard, E. Baron, D. Mihalas, G. Shaviv, S. Shore, S. Starrfield, H. Störzer, and R. Wehrse for stimulating and helpful discussions and the anonymous referee for many helpful comments on an earlier draft of this paper. P. H. H. acknowledges partial support from a NASA LTSA grant to ASU. L. M. E. thanks A. Burrows for his generous support through grant NAGW-2145 from NASA under the LTSARP and acknowledges an allotment of CPU time on the ASU Nova Group IBM RS/6000 cluster, obtained with partial support from the NSF.

REFERENCES

Abbott, D. C., & Lucy, L. B. 1985, ApJ, 288, 679
Allard, F. 1993, private communication
Arnett, W. D. 1991a, ApJ, 383, 295
———. 1991b, private communication
Baron, E., & Hauschildt, P. H. 1994, in preparation
Catchpole, R. M., et al. 1987, MNRAS, 229, 15P
Cox, A. N., & Stewart, J. N. 1970a, AJS, 19, 243
———. 1970b, AJS, 19, 261
Eastman, R. G., & Kirshner, R. P. 1989, ApJ, 347, 771
Eastman, R. G., Woosley, S. E., Weaver, T. A., & Pinto, P. A. 1993, ApJ, submitted
Ensman, L. 1991, Ph.D. thesis, Univ. California, Santa Cruz
Ensman, L., & Burrows, A. 1992, ApJ, 393, 742
Ensman, L., Hauschildt, P. H., & Allard, F. 1993, in preparation
Hauschildt, P. H. 1992a, JQSRT, 47, 433
———. 1992b, ApJ, 398, 224
———. 1993, JQSRT, 50, 301
Hauschildt, P. H., Starrfield, S., Austin, S., Wagner, R. M., Shore, S. N., & Sonneborn, G. 1994, ApJ, in press
Hauschildt, P. H., & Wehrse, R. 1991, JQSRT, 46, 81
Hauschildt, P. H., Wehrse, R., Starrfield, S., & Shaviv, G. 1992, ApJ, 393, 307
Höflich, P. 1987, in Proc. ESO Workshop on the SN 1987A, ed. I. J. Danziger (ESO Conf. and Workshop Proc. 26), (Garching: ESO), 449
———. 1988, in Proc. Astron. Soc. Australia, 7, 434
———. 1990, Habilitation thesis, Ludwig-Maximilians-Universität, Munich
Höflich, P., Müller, E., & Khokhlov, A. 1993, A&A, 268, 570
Johnson, L. C. 1972, ApJ, 174, 227
Karp, A. H., Lasher, G., Chan, K. L., & Salpeter, E. E. 1977, ApJ, 214, 161
Kurucz, R. L. 1988, private communication
Kurucz, R. L., & Peytremann, E. 1975, Smithsonian Astrophys. Obs. Spec. Rep. 362
Lucy, L. B. 1987a, in Proc. ESO Workshop on the SN 1987A, ed. I. J. Danziger (ESO Conf. Workshop Proc. 26) (Garching: ESO), 417
———. 1987b, A&A, 182, L31
Mihalas, D. 1978, Stellar Atmospheres (San Francisco: Freeman)
———. 1986, in Astrophysical Radiation Hydrodynamics, ed. K.-H. A. Winkler & M. L. Norman (Dordrecht: Reidel), 45
Mihalas, D., Kunasz, P. B., & Hummer, G. 1976, ApJ, 206, 515
Mihalas, D., & Mihalas, B. W. 1984, Foundations of Radiation Hydrodynamics (Oxford: Oxford Univ. Press)
Müller, E., & Höflich, P. 1991, in SN 1987A and Other Supernovae, ed. I. J. Danziger & K. Kjär (Garching: ESO), 379
Phillips, M. M., Heathcote, S. R., Hamuy, M., & Navarette, M. 1988, AJ, 95, 1987
Schmutz, W., Abbott, D. C., Russell, R. S., Hamann, W.-R., & Wessolowski, U. 1990, ApJ, 355, 255
Shine, R. A. 1973, Ph.D. thesis, Univ. Colorado
Shine, R. A., & Linsky, J. L. 1974, Sol. Phys., 39, 49
Woosley, S. E. 1988, ApJ, 330, 218